

1 **Structure and stress field of the lithosphere between**  
2 **Pamir and Tarim**

3 **Wasja Bloch<sup>1\*</sup>, Bernd Schurr<sup>1</sup>, Xiaohui Yuan<sup>1</sup>, Lothar Ratschbacher<sup>2</sup>,**  
4 **Sanaa Reuter<sup>2</sup>, Sofia-Katerina Kufner<sup>1,3</sup>, Qiang Xu<sup>4,5</sup>, Junmeng Zhao<sup>4,5</sup>**

5 <sup>1</sup>GFZ German Research Centre for Geosciences, 14473 Potsdam, Germany

6 <sup>2</sup>Geologie, Technische Universität Bergakademie Freiberg, 09599 Freiberg, Germany

7 <sup>3</sup>British Antarctic Survey, Cambridge CB3 0ET, England

8 <sup>4</sup>Key Laboratory of Continental Collision and Plateau Uplift, Institute of Tibetan Plateau Research,

9 Chinese Academy of Sciences, Beijing 100101, China

10 <sup>5</sup>CAS Center for Excellence in Tibetan Plateau Earth Sciences, Beijing 100101, China

11 **This manuscript is a non-peer reviewed preprint submitted to EarthArXiv.**  
12 **Submitted to *Geophysical Research Letters* (Wiley)**

13 **Key Points:**

- 14 • New local earthquake catalog and seismic velocity model for the Pamir-plateau  
15 region
- 16 • Elevated velocities outline the northern and eastern margins of the Indian man-  
17 tle indenter beneath the Pamir plateau
- 18 • Indenter overturns the eastern end of the Asian slab and terminates along a trans-  
19 form margin against the Tarim block

---

\*Now at: Earth, Ocean and Atmospheric Sciences, University of British Columbia, Vancouver, Canada.

Corresponding author: Wasja Bloch, [wbloch@eoas.ubc.ca](mailto:wbloch@eoas.ubc.ca)

**Abstract**

The Pamir plateau protrudes  $\sim 300$  km between the Tajik- and Tarim-basin lithosphere of Central Asia. Whether its salient location and shape are caused by forceful indentation of a promontory of Indian mantle lithosphere is debated. We present a new local-seismicity and focal-mechanism catalog, and a P-wave velocity model of the eastern part of the collision system. The data outline a south-dipping Asian slab that overturns in its easternmost segment. The largest principal stress at depth acts normal on the slab and is orientated parallel to the plate convergence direction. In front (south) of the Asian slab, a volume of mantle with elevated velocities and lined by weak seismicity constitutes the postulated Indian mantle indenter. The indenter delaminates and overturns the Asian slab, underthrusts the Tarim lithosphere along a compressive transform boundary, and controls the location and shape of the Pamir plateau.

**Plain Language Summary**

The Pamir plateau stands out distinctively between the Tajik basin to the west and the Tarim basin to the east. Its location and shape is either caused by a part of the Indian continent that protrudes below Pamir's crust, or thinned lithosphere of a former Asian basin existed in place of the Pamir and subducted during the collision of India with Asia. Our new seismological data show that the Asian slab, that is a displaced part or slice of the Tarim–Tajik-basin lithosphere, is overturned beneath the eastern Pamir. A zone of high seismic velocities, indicative of a relatively cold and rigid mantle lithosphere, occurs in front (south) of the Asian slab. A seismically active zone with low seismic velocities is squeezed between this structure and the Tarim lithosphere. Together, these observations trace the northern and eastern margin of the Indian mantle indenter that predefines the shape of the Pamir plateau.

**1 Introduction**

The salient Pamir plateau is part of the India-Asia collision system. It is offset by  $\sim 300$  km to the north in the relation to the adjacent Tibet plateau and protrudes between the Tajik basin in the west and the cratonic block of the Tarim basin in the east (e.g. Lu et al., 2008). The northern Pamir and the Kunlun of northwestern Tibet comprise subduction-accretion-arc complexes accreted to and built on Asian continental basement. The central and southern Pamir and the Karakorum and Hindu-Kush represent Gondwana-derived microcontinents and subduction-accretion-arc complexes (Fig. 1; Burtman & Molnar, 1993; Schwab et al., 2004).

Beneath the Pamir, a band of intermediate-depth (50–250 km) earthquakes, that extends from the southwestern Pamir northeastward into the central Pamir, bends eastward, and shows diminished earthquake activity beneath the eastern Pamir (Fig. 2; Pegler & Das, 1998; Sippl, Schurr, Yuan, et al., 2013). Receiver function images, seismic tomography, and the analysis of guided waves show that the earthquakes in the western and central Pamir reside in a 10–15 km thick, E- to S-dipping low velocity zone (LVZ) connected to the Asian lithosphere; seismic velocities indicate that the LVZ represents continental crust, constituting—together with the underlying mantle lithosphere—the Asian slab (Schneider et al., 2013; Sippl, Schurr, Tymphel, et al., 2013; Mechie et al., 2019). Beneath the northwestern Kunlun, diffuse seismicity at 100–150 km depth was attributed to Tarim lithosphere underthrusting the Pamir (Fan et al., 1994; Pegler & Das, 1998).

To understand the oroclinal shape of the Pamir, the intricate intermediate-depth seismicity beneath the Hindu-Kush, Pamir, and Kunlun, and the along-strike changes of the deep structure from the Hindu-Kush through the Pamir to Tibet and the Himalaya, it is a key to know whether Asian lithosphere subducts as a narrow, back-rolling slab of thinned crust (Burtman & Molnar, 1993; Sobel et al., 2013) or Asian lower crust and man-

69 tle lithosphere is forced to subduct/delaminate due to indentation by cratonic Indian man-  
70 tle lithosphere (Kufner et al., 2016; Metzger et al., 2017). If an indenter governs the shape  
71 of the Pamir plateau, its properties can best be characterized at its margins, where it  
72 interacts with and has a detectable contrast to the bounding units. For the western mar-  
73 gin, Kufner et al. (2016, 2018) argued that a sinistral-oblique transform margin separates  
74 indenting cratonic Indian mantle lithosphere beneath the Pamir from subducting Indian  
75 continental-margin lithosphere below the Hindu-Kush. The subduction model postulates  
76 rollback of a narrow Asian slab of thinned continental crust that involves mantle cor-  
77 ner flow and a subduction-transform edge propagator fault, separating the subducting  
78 Asian slab and its hanging wall from the Tarim block to the east. Geophysical data indi-  
79 cate that the hinterland crust is not thinned ( $>50$  km; Schneider et al., 2019), ques-  
80 tioning the premise of the rollback model, because thick buoyant continental crust typi-  
81 cally does not subduct beneath a continent as a whole (e.g. Z.-H. Li et al., 2016; Kelly  
82 & Beaumont, 2021). The indentation model involves forced Asian slab subduction and  
83 delamination due to flat-slab underthrusting of a mechanically-strong Indian continen-  
84 tal lithospheric mantle indenter, a process recently modeled for the Pamir (Kelly & Beau-  
85 mont, 2021). The indenter is imaged by refraction seismology and local body wave to-  
86 mography as a high velocity zone (HVZ) south of the Asian slab (Mechie et al., 2012;  
87 Sippl, Schurr, Tympel, et al., 2013). Teleseismic body and surface wave tomography shows  
88 that it connects with the exposed Indian craton (e.g. C. Li et al., 2008; Agius & Lebe-  
89 dev, 2013; van Hinsbergen et al., 2019; Liang et al., 2020); its northern extent remained  
90 unresolved due to the smearing of the indenter HVZ with the HVZ that represents cra-  
91 tonic Asia.

92 Herein, intermediate-depth earthquakes, focal-mechanism based stress data, and  
93 a P-wave velocity model derived from new and published local seismological data in com-  
94 panionship with new receiver functions (Xu et al., 2021) illuminate the lithospheric con-  
95 figuration of the central and eastern Pamir and the boundary zone with the Tarim cra-  
96 ton. Our data characterize the northern tip of an indenter—interpreted as a promontory  
97 of Indian mantle lithosphere—and its eastern edge, where it underthrusts on the litho-  
98 sphere of the Tarim block.

## 99 **2 Data and Methods**

100 We used seismograms recorded with two new local seismic networks that were in  
101 operation between August 2015 and July 2017 in the eastern Pamir, northwestern Kun-  
102 lun, and northwestern Tarim basin (Text S1; Yuan, Schurr, Bloch, et al., 2018; Yuan,  
103 Schurr, Kufner, & Bloch, 2018) and additional regional stations (PMP International (Tajik-  
104 istan), 2005; SEISDMC, 2021). We detected seismic events using a waveform–envelope–  
105 coherence-based approach (Comino et al., 2017) and picked P- and S-wave arrival times  
106 using calibrated automatic picking algorithms (Text S2; Aldersons, 2004; Diehl et al.,  
107 2009).

108 Using additional data of an existing earthquake catalog from the western and cen-  
109 tral Pamir (Sippl, Schurr, Tympel, et al., 2013), we inverted for the 3-D subsurface P-  
110 wave velocity structure (Thurber, 1983). We masked out poorly resolved volumes of the  
111 tomogram based on a checkerboard resolution test and performed synthetic recovery tests  
112 for the anomalies that are most important to our interpretation (Text S3; Fig. S1–S10).

113 We jointly located the newly and previously (Sippl, Schurr, Tympel, et al., 2013)  
114 detected seismicity at intermediate depth in the 3-D velocity model, assessed location  
115 uncertainties (Lomax et al., 2000) and performed a relative event relocation for events  
116 that were  $<10$  km apart (Waldhauser & Ellsworth, 2000) (Text S4; Fig. S11–S14), yield-  
117 ing a unified catalog of 1,493 events at intermediate depth.

118 We determined focal mechanisms of the strongest of the newly located events and  
 119 inverted for stress directions, stress tensor shape factors and uncertainties (Text S5; Fig. S15).  
 120 The seismicity catalog (Data Set S1), focal mechanism catalog (Data Set S2), and the  
 121 velocity structure (Data Set S3) are published in the Supplemental Material.

### 122 3 Seismicity

123 Crustal seismicity of the upper 30 km is dominated by the aftershock sequences of  
 124 strong earthquakes that struck the Pamir in 2015/16 and is omitted from the main fig-  
 125 ures. The middle and lower crust (30–50 km depth) is essentially aseismic (Fig. S2). Intermediate-  
 126 depth earthquakes in the central and eastern Pamir could be localized with a median (5%–  
 127 95% quantile) uncertainty of 2.3 (1.1–6.4) km in longitudinal direction, 2.0 (1.0–5.0) km  
 128 in latitude and 3.2 (1.8–9.4) km in depth (Fig. S14). They outline three steeply-dipping,  
 129 planar to curvilinear segments separated by regions of sparse seismicity (Fig. 2; Fig. 3).

130 Segment 1 begins at 72.8°E, 38°N, in continuation of the NE-striking, planar, seis-  
 131 mically active structure farther to the southwest (Fig. 2; Schneider et al., 2013; Sippl,  
 132 Schurr, Yuan, et al., 2013). It forms an S- to SE-dipping band between 73°E and 74.3°E,  
 133 and shows vigorous seismicity between 70–180 km depth in its easternmost part (Fig. 3A;  
 134 Fig. S11); farther east, seismic activity decreases.

135 Segment 2 in the eastern Pamir—in the direct continuation of segment 1—contains  
 136 a few earthquakes at 50–80 km depth in a S-dipping structure. Below, at 80–170 km depth,  
 137 the earthquake-defined band dips N (Fig. 2, dotted lines in Fig. 3B; Fig. S13g-i). Seis-  
 138 micity in segment 2 is less intense compared to segment 1 (Fig. S11).

139 Seismicity in segment 3 forms a continuous, NNW-striking structure at 80–120 km  
 140 depth between 37°N and 38°N; it follows the northwestern Kunlun (Fig. 2; Fig. 3C). Seis-  
 141 mic activity is comparably weak (Fig. S11).

142 In all segments, focal mechanisms show dominantly thrust and subordinately strike-  
 143 slip faulting. Accordingly, the regional stress tensor at intermediate depth indicates a  
 144 thrust regime with a near-horizontal largest principal stress,  $\sigma_1$ , trending N13°W±60°  
 145 (95% confidence interval) and near vertical  $\sigma_3$  (Fig. 2). Inverting for the stress of the three  
 146 segments separately yields similar directions, despite strongly variable uncertainties due  
 147 to the disparate amounts of data (Fig. S15). The azimuth of  $\sigma_1$  is about parallel to the  
 148 azimuth of the GNSS vectors in the southern and central Pamir (south of 38.8°N), N12°W±4°  
 149 (Fig. 2; Ischuk et al., 2013; Zubovich et al., 2010).

### 150 4 Velocity Structure

151 In the shallow crust, the sediment fill of the Tarim basin forms a LVZ (<5 km/s,  
 152 *TL* in Figs. 3B–D). In the middle–lower crust, the Tarim basement appears as a discon-  
 153 tinuous HVZ (6.5–7.5 km/s, *TH* in Fig. 3C, Fig. 3E) close to the poor-resolution rim  
 154 of the tomographic volume. A LVZ is located in the mantle of northwestern Tarim (*AL*  
 155 in Fig. 3G). An arcuate crustal LVZ extends below the northern Pamir, the Kongur Ex-  
 156 tensional System, and the northwestern Kunlun (5–6 km/s, *PL* in Figs. 3A–C and 3E).  
 157 It is sandwiched between the Tarim basement HVZ, *TH*, and another crustal HVZ in  
 158 the central Pamir (6–7 km/s, *PH* in Fig. 3A; Fig. 3E). Recovery tests indicate that *PH*  
 159 and *PL* can be resolved under the given ray geometry and are not smearing artifacts from  
 160 the velocity anomalies below (Fig. S10a and b).

161 At mantle depths, dipping LVZs are located above the seismicity in segments 1–3  
 162 (7–8 km/s, *L1*, *L2*, *L3* in Figs. 3A–C and 3F). The LVZs *L2* and *L3* of segments 2 and 3  
 163 appear continuous in map view (Fig. 3F), but are separated by the seismicity of segment  
 164 2 (Fig. 3B). The seismically active structures are underlain by HVZs (8.5–9.5 km/s, *H1*,  
 165 *H2*, *H3* in Figs. 3A–C and 3G) and have the same dip as the LVZs above. The contrast

166 between the LVZs and the underlying HVZs is well resolved (Fig. S10a, b, d). The lo-  
 167 cation and dip of  $L2$  and  $L3$  coincide with Moho troughs identified in receiver functions  
 168 (Fig S16; Xu et al., 2021), substantiating our observations. The HVZs are resolved to  
 169 a depth of 105–120 km (Fig. S10b and d). In segment 1 and 2, the HVZs  $H1$  and  $H2$  are  
 170 continuous along strike below  $\sim 105$  km depth (Fig. 3G). In segment 2,  $H2$  and  $H3$  touch,  
 171 but are separated by seismicity in the same way as  $L2$  and  $L3$  (Fig. 3B; Fig. 3G). The  
 172 LVZs and HVZs of segment 1 ( $L1$  and  $H1$ ; Fig. 3A) and segment 3 ( $L3$  and  $H3$ ; Fig. 3C)  
 173 dip in the same direction as the seismicity structures.

## 174 5 Interpretation and Discussion

175 We visualize our interpretation of the lithospheric architecture of the central and  
 176 eastern Pamir in the block diagram of Figure 4. Sippl, Schurr, Tympel, et al. (2013) in-  
 177 ferred eclogitization of the lower crust of segment 1 due to the sinking of the Asian slab  
 178 and that this lower crust hosts the band of intermediate-depth earthquakes; in our to-  
 179 mogram, we interpret the LVZ  $L1$  as the lower crust and the HVZ  $H1$  as the mantle litho-  
 180 sphere of the Asian slab (Fig. 3A). Eclogitization has been found to excite seismicity in  
 181 oceanic subduction regimes (Incel et al., 2017; Kita et al., 2006; Yuan et al., 2000), as  
 182 well as in continental lower crustal rocks (Incel et al., 2019; Jamtveit et al., 2018; John  
 183 et al., 2009). Upon eclogitization, the crust becomes indistinguishable from the surround-  
 184 ing mantle in terms of seismic velocities (Rondenay et al., 2008), creating the observed  
 185 characteristic pattern of a LVZ shaping a local Moho trough that disappears at larger  
 186 depths where seismicity starts. The aseismic mid-crustal LVZ  $PL$  (Figs. 3A–C and 3E;  
 187 see also W. Li et al., 2018; Sippl, Schurr, Tympel, et al., 2013), may represent a heated  
 188 rock volume, for example developed by excess radiogenic heat production in the thicken-  
 189 ed crust or viscous dissipation due to ongoing continental collision (e.g. Bird et al.,  
 190 1975; Burg & Gerya, 2005). We consider heating due to asthenospheric inflow, as would  
 191 be expected in the hanging wall of a S-dipping subduction zone, as unlikely, because the  
 192 tomogram does not show a LVZ south of the seismic zone; in contrast, subcrustal P-wave  
 193 velocities are  $>8$  km/s with large HVZs ( $>8.5$  km/s) embedded (e.g.,  $H3$ ), indicating rel-  
 194 atively cold and rigid lithospheric mantle south of the Asian slab.

195 We interpret segment 2 as the eastern continuation of segment 1 of the Asian slab,  
 196 because of the similar depth extent of the seismic zone and the continuity of the under-  
 197 lying HVZ (Fig. 2; Figs. 3A, 3B, and 3G). If instead segment 2 is separated from seg-  
 198 ment 1 and forms a continuous unit with segment 3, the Asian slab would terminate at  
 199  $\sim 74.5^\circ\text{E}$  and the along-strike correlation of seismicity and HVZs ( $H1$  and  $H2$ ) between  
 200 segments 1 and 2 would be a coincidence. The N-dip of the seismically active segment  
 201 2 can be traced  $\sim 100$  km along strike in narrowly-adjoining profiles between  $75.1$  to  $75.9^\circ\text{E}$   
 202 (Fig. S13g-j) and is robust with respect to the choice of the velocity model (Fig. S12g-  
 203 j). When representing the Asian slab, this seismicity pattern indicates overturning be-  
 204 low  $\sim 80$  km depth (Fig. 2; Fig. 3B). Overturning in turn indicates that a force acts nor-  
 205 mal to the slab, which we expect in the presence of a pushing indenter. We attribute the  
 206 seismicity gap between segments 1 and 2 to a slab tear that may explain how the slab  
 207 dip changes over a relatively short distance ( $\sim 40$  km). In our interpretation, the Asian  
 208 slab terminates in a seismicity cluster below the Kashgar-Yecheng Transfer System at  
 209  $76.2^\circ\text{E}$  (Fig. 2), where, in a delamination scenario, it would need to be torn off Tarim’s  
 210 lithosphere to the east, where it would have originally been attached to.

211 In the northwestern Kunlun, the seismicity band of segment 3, the LVZ  $L3$ , and  
 212 the HVZ  $H3$  show the characteristic eclogitization pattern we inferred for segments 1  
 213 and 2. The structure dips  $\sim\text{ENE}$  and descends from the base of the Pamir crust in front  
 214 of segment 2, a geometry that is also imaged by receiver functions (Fig. S16; Xu et al.,  
 215 2021). This geometry is inconsistent with a semicircular, amphitheater-like continuation  
 216 of the Asian slab below Kunlun, but requires association of seismicity and the velocity  
 217 anomalies with another tectonic unit (see below).

218 The orientation of  $\sigma_1$  at depth indicates that a N13°W compressive stress field acts  
 219 on the deep structure of the Pamir. The stress orientation is stable across the three seg-  
 220 ments (Fig. S15), although uncertainty for the individual segments may become signif-  
 221 icant, due to the varying data availability. In contrast, N–S extension should occur south  
 222 of the slab (in segment 3) if deformation was otherwise governed by a narrow Asian slab  
 223 rolling back northward. We note that compressive stresses are sub-parallel to the N12°W( $\pm 8^\circ$ )-  
 224 oriented surface velocity of the southern and central Pamir crust (e.g. Zubovich et al.,  
 225 2010; Ischuk et al., 2013; Metzger et al., 2020). Both are deflected about 15° counter-  
 226 clockwise from the N4°E-oriented convergence direction between India and Asia (DeMets  
 227 et al., 1994). Parallelism of the orientation of southern and central Pamir’s surface dis-  
 228 placement between the Sarez-Karakul fault system and the Kongur extensional system  
 229 with  $\sigma_1$  at depth suggests that crustal movement is prescribed by the mantle stresses,  
 230 with the mantle lithosphere dragging the overlying Pamir crust south of the Asian slab  
 231 northward, offering a straightforward explanation. For segments 1 and 2, parallelism of  
 232  $\sigma_1$  and surface displacement vectors arises naturally if collision occurs at an indenter tip.

233 In concert with the lack of thinned hinterland crust (Schneider et al., 2019) and  
 234 the imaging of a HVZ at  $\sim 200$  km depth that connects with the exposed Indian craton  
 235 below the Pamir-Karakorum (C. Li et al., 2008; Agius & Lebedev, 2013; van Hinsber-  
 236 gen et al., 2019), the following of our observations support the presence of an indenter  
 237 below the Pamir: (1) the repeated detection of HVZ *H3* south of the Asian slab (this  
 238 study; Mechie et al., 2012; Sippl, Schurr, Tymphel, et al., 2013) that excludes astheno-  
 239 spheric inflow above a S-dipping, back-rolling subduction zone; (2) the overturned geo-  
 240 metry of segment 2, indicated by a change in the dip of the seismic zone in profile view  
 241 and by the along-strike correlation with segment 1; (3) the NNW–SSE compressive stress  
 242 field across the central and eastern Pamir at mantle depth (50–100 km) that is parallel  
 243 to surface displacement.

244 The indenter is most likely cratonic Indian lithosphere, because the Gondwana-terrane  
 245 lithosphere of the central and southern Pamir and Karakorum terranes would be too weak  
 246 to transmit enough force to delaminate and overturn the Asian slab (Kelly & Beaumont,  
 247 2021). We locate the delamination front at the base of the rheologically weak mid-crustal  
 248 LVZ *PL* (red line in Fig. 4), just north of the Asian slab. The present location and form  
 249 of the Pamir and the Asian slab is in this interpretation governed by the shape of the  
 250 indenter. Additional structural complexity, such as the location of slab tears or turn-overs,  
 251 may be due to lateral changes in the strength of the indented Asian lithosphere or the  
 252 along-strike variability of the indenter tip (Z.-H. Li et al., 2016; Kelly & Beaumont, 2021).  
 253 For example, the mid-crustal HVZ *PH*, which overlies a distinctive Moho bulge in seg-  
 254 ment 1 (Fig 3A; Schneider et al., 2019), may represent a lithosphere-scale anticline; in  
 255 segment 1, the top of the indenter appears to rise higher than in segment 2 and in par-  
 256 ticular in segment 3 (Fig. 4).

257 The ENE-dipping Moho trough (Fig. S16; Xu et al., 2021) and velocity anomalies  
 258 (*L3* and *H3*) can, in this scenario, be interpreted as Pamir crust and indenter mantle  
 259 lithosphere that underthrusts the Asian (Tarim) mantle lithosphere (Fig. 3C). The earth-  
 260 quakes may, as in the Asian slab, occur in thickened crust undergoing eclogitization (John  
 261 et al., 2009; Incel et al., 2019). This crust is likely dragged to depth between the bull-  
 262 dozing indenter and the margin of the Tarim block. The stress field of the earthquakes  
 263 inside the underthrusting crust *L3* indicates that it moves with the NNW-ward moving  
 264 indenter and underthrusts the Tarim hanging wall at a highly oblique angle. As the to-  
 265 mographic and receiver function Moho both dip  $\sim$ WSW beneath the northwestern Kun-  
 266 lun east of LVZ *L3* (Fig. 3C; Xu et al., 2021), we infer that Tarim underthrusts the north-  
 267 western Kunlun as well, building a stack of (from top to bottom) Kunlun–Tarim–Pamir  
 268 crust (Fig. 4C). This excess crust may be responsible for a positive anomaly in the iso-  
 269 static gravity residual (20-mGal-contour in Fig. 2; Balmino et al., 2012) that flanks the

270 northern edge of the Tibet plateau (Fig. 2, inset), and was interpreted to represent thrust-  
 271 ing of Tarim crust under the western and central Kunlun (Wittlinger et al., 2004).

272 The herein deduced configuration of the tectonic units and the transpressive stress  
 273 field in the intermediate-depth seismic zone of segment 3 outlines a compressive litho-  
 274 spheric transform boundary as the plate boundary between the Indian indenter and the  
 275 Tarim block (Fig. 4). It changes to a forced subduction/delamination boundary due to  
 276 indentation under the central Pamir. The tear that separates the Asian slab from Tarim  
 277 propagates northward with the advancing indenter. Indentation may have caused the  
 278 capture and dragging along of the crust from the collision system into the transform zone  
 279 (Fig. 4C). The transform margin likely transitions southeastward into a subduction plate  
 280 boundary where the Tarim block underthrusts the western Tibet plateau (Wittlinger et  
 281 al., 2004). Our interpretation of the deep structure suggests a strong along-strike seg-  
 282 mentation of the northern tip of the Indian plate; it subducts under the Hindu-Kush (Kufner  
 283 et al., 2021), indents in the Pamir (this study; Kufner et al., 2016) and has variable dip  
 284 angles and locations in the rest of Tibet (e.g. Zhao et al., 2010).

## 285 6 Conclusion

286 We located zones of intermediate-depth seismicity in the central and eastern Pamir  
 287 and northwestern Kunlun, established their geometries, determined the principal stress  
 288 orientations, and computed a seismic velocity model of the subsurface. We traced a sub-  
 289 ducting/delaminating Asian slab eastward as far as the western edge of the Tarim block  
 290 and showed that the eastern segment of the slab is overturned and torn from the cen-  
 291 tral one. Together with the presence of a high velocity zone in front (south) of the Asian  
 292 slab and the parallelism of the largest principal stress at depth with the surface displace-  
 293 ment across the eastern and southern Pamir, we interpret this geometry as indicating  
 294 underthrusting of Indian mantle lithosphere beneath the Pamir plateau and delamina-  
 295 tion of the Asian slab. A slice of lower crust is dragged along with the indenter and smeared  
 296 into the compressive transform boundary between the indenter and the Tarim block at  
 297 depth.

## 298 Acknowledgments

299 We thank the drivers and field participants from the Institute of Tibetan Plateau Re-  
 300 search, especially Hongbing Liu, who helped to organize the station deployment, and Chris-  
 301 tian Sippl for sharing code and discussion. Funded by the CaTeNA project of the Ger-  
 302 man Federal Ministry of Science and Education (support codes 03G0878A and 03G0878B)  
 303 and German Research Council (DFG) grant Ra 442/41. Seismic data was handled us-  
 304 ing *obspy* (Krischer et al., 2015) and *pyrocko* (Heimann et al., 2017). Figures were cre-  
 305 ated with the help of the *Generic Mapping Tools* (Wessel et al., 2013) and *matplotlib* (Hunter,  
 306 2007), using *scientific color-maps* (Cramer et al., 2020). Part of the instruments were  
 307 provided by GIPP of GFZ Potsdam. Seismic data are archived by GEOFON data cen-  
 308 ter.

## 309 References

- 310 Agius, M. R., & Lebedev, S. (2013). Tibetan and Indian lithospheres in the upper  
 311 mantle beneath Tibet: Evidence from broadband surface-wave dispersion. *Geo-*  
 312 *chemistry, Geophysics, Geosystems*, *14*(10), 4260–4281.
- 313 Aldersons, F. (2004). Toward three-dimensional crustal structure of the Dead Sea re-  
 314 gion from local earthquake tomography. *PhD thesis*.
- 315 Balmino, G., Vales, N., Bonvalot, S., & Briais, A. (2012). Spherical harmonic mod-  
 316 elling to ultra-high degree of Bouguer and isostatic anomalies. *Journal of*  
 317 *Geodesy*, *86*(7), 499–520.

- 318 Bird, P., Toksöz, M. N., & Sleep, N. H. (1975). Thermal and mechanical mod-  
 319 els of continent-continent convergence zones. *Journal of Geophysical Research*,  
 320 *80*(32), 4405–4416.
- 321 Burg, J.-P., & Gerya, T. (2005). The role of viscous heating in Barrovian metamor-  
 322 phism of collisional orogens: thermomechanical models and application to the  
 323 Lepontine Dome in the Central Alps. *Journal of Metamorphic Geology*, *23*(2),  
 324 75–95.
- 325 Burtman, V. S., & Molnar, P. H. (1993). *Geological and geophysical evidence for*  
 326 *deep subduction of continental crust beneath the Pamir* (Vol. 281). Geological  
 327 Society of America.
- 328 Comino, J. Á. L., Heimann, S., Cesca, S., Milkereit, C., Dahm, T., & Zang, A.  
 329 (2017). Automated full waveform detection and location algorithm of acoustic  
 330 emissions from hydraulic fracturing experiment. *Procedia engineering*, *191*,  
 331 697–702.
- 332 Cramer, F., Shephard, G. E., & Heron, P. J. (2020). The misuse of colour in science  
 333 communication. *Nature communications*, *11*(1), 1–10.
- 334 DeMets, C., Gordon, R. G., Argus, D. F., & Stein, S. (1994). Effect of recent re-  
 335 visions to the geomagnetic reversal time scale on estimates of current plate  
 336 motions. *Geophysical research letters*, *21*(20), 2191–2194.
- 337 Diehl, T., Deichmann, N., Kissling, E., & Husen, S. (2009). Automatic S-wave  
 338 picker for local earthquake tomography. *Bulletin of the Seismological Society of*  
 339 *America*, *99*(3), 1906–1920.
- 340 Fan, G., Ni, J. F., & Wallace, T. C. (1994). Active tectonics of the Pamirs and  
 341 Karakorum. *Journal of Geophysical Research: Solid Earth*, *99*(B4), 7131–  
 342 7160.
- 343 Heimann, S., Kriegerowski, M., Isken, M., Cesca, S., Daout, S., Grigoli, F., ... oth-  
 344 ers (2017). Pyrocko-An open-source seismology toolbox and library. *GFZ Data*  
 345 *Services*. doi: 10.5880/GFZ.2.1.2017.001
- 346 Hunter, J. D. (2007). Matplotlib: A 2D graphics environment. *Computing in Science*  
 347 *& Engineering*, *9*(3), 90–95. doi: 10.1109/MCSE.2007.55
- 348 Incel, S., Hilaret, N., Labrousse, L., John, T., Deldicque, D., Ferrand, T., ... Schub-  
 349 nel, A. (2017). Laboratory earthquakes triggered during eclogitization of  
 350 lawsonite-bearing blueschist. *Earth and Planetary Science Letters*, *459*, 320–  
 351 331.
- 352 Incel, S., Labrousse, L., Hilaret, N., John, T., Gasc, J., Shi, F., ... others (2019).  
 353 Reaction-induced embrittlement of the lower continental crust. *Geology*, *47*(3),  
 354 235–238.
- 355 Ischuk, A., Bendick, R., Rybin, A., Molnar, P., Khan, S. F., Kuzikov, S., ... others  
 356 (2013). Kinematics of the Pamir and Hindu Kush regions from GPS geodesy.  
 357 *Journal of geophysical research: solid earth*, *118*(5), 2408–2416.
- 358 Jamtveit, B., Ben-Zion, Y., Renard, F., & Austrheim, H. (2018). Earthquake-  
 359 induced transformation of the lower crust. *Nature*, *556*(7702), 487–491.
- 360 John, T., Medvedev, S., Rüpke, L. H., Andersen, T. B., Podladchikov, Y. Y., &  
 361 Austrheim, H. (2009). Generation of intermediate-depth earthquakes by  
 362 self-localizing thermal runaway. *Nature Geoscience*, *2*(2), 137–140.
- 363 Kelly, S., & Beaumont, C. (2021). Balanced Cross-Sections and Numerical Model-  
 364 ing of the Lithospheric-Scale Evolution of the Hindu Kush and Pamir. *Journal*  
 365 *of Geophysical Research: Solid Earth*, *126*(3), e2020JB020678.
- 366 Kita, S., Okada, T., Nakajima, J., Matsuzawa, T., & Hasegawa, A. (2006). Existence  
 367 of a seismic belt in the upper plane of the double seismic zone extending in the  
 368 along-arc direction at depths of 70–100 km beneath NE Japan. *Geophysical*  
 369 *Research Letters*, *33*(24).
- 370 Krischer, L., Megies, T., Barsch, R., Beyreuther, M., Lecocq, T., Caudron, C., &  
 371 Wassermann, J. (2015). ObsPy: A bridge for seismology into the scientific  
 372 Python ecosystem. *Computational Science & Discovery*, *8*(1), 014003.



- 373 Kufner, S.-K., Kakar, N., Bezada, M., Bloch, W., Metzger, S., Yuan, X., . . . oth-  
 374 ers (2021). The Hindu Kush slab break-off as revealed by deep structure and  
 375 crustal deformation. *Nature communications*, *12*(1), 1–11.
- 376 Kufner, S.-K., Schurr, B., Ratschbacher, L., Murodkulov, S., Abdulhameed, S.,  
 377 Ischuk, A., . . . Kakar, N. (2018). Seismotectonics of the Tajik basin and  
 378 surrounding mountain ranges. *Tectonics*, *37*(8), 2404–2424.
- 379 Kufner, S.-K., Schurr, B., Sippl, C., Yuan, X., Ratschbacher, L., Ischuk, A., . . .  
 380 others (2016). Deep India meets deep Asia: Lithospheric indentation, delami-  
 381 nation and break-off under Pamir and Hindu Kush (Central Asia). *Earth and*  
 382 *Planetary Science Letters*, *435*, 171–184.
- 383 Li, C., Van der Hilst, R. D., Meltzer, A. S., & Engdahl, E. R. (2008). Subduction  
 384 of the Indian lithosphere beneath the Tibetan Plateau and Burma. *Earth and*  
 385 *Planetary Science Letters*, *274*(1-2), 157–168.
- 386 Li, W., Chen, Y., Yuan, X., Schurr, B., Mechie, J., Oimahmadov, I., & Fu, B.  
 387 (2018). Continental lithospheric subduction and intermediate-depth seis-  
 388 micity: Constraints from S-wave velocity structures in the Pamir and Hindu  
 389 Kush. *Earth and Planetary Science Letters*, *482*, 478–489.
- 390 Li, Z.-H., Liu, M., & Gerya, T. (2016). Lithosphere delamination in continental  
 391 collisional orogens: A systematic numerical study. *Journal of Geophysical Re-*  
 392 *search: Solid Earth*, *121*(7), 5186–5211.
- 393 Liang, Y., Li, L., Liao, J., & Gao, R. (2020). Interaction of the Indian and Asian  
 394 plates under the Pamir and Hindu-Kush regions: Insights from 3-D shear wave  
 395 velocity and anisotropic structures. *Geochemistry, Geophysics, Geosystems*,  
 396 *21*(8), e2020GC009041.
- 397 Lomax, A., Virieux, J., Volant, P., & Berge-Thierry, C. (2000). Probabilistic earth-  
 398 quake location in 3D and layered models. In *Advances in seismic event location*  
 399 (pp. 101–134). Springer.
- 400 Lu, S., Li, H., Zhang, C., & Niu, G. (2008). Geological and geochronological evi-  
 401 dence for the Precambrian evolution of the Tarim Craton and surrounding  
 402 continental fragments. *Precambrian Research*, *160*(1-2), 94–107.
- 403 Mechie, J., Schurr, B., Yuan, X., Schneider, F., Sippl, C., Minaev, V., . . . others  
 404 (2019). Observations of guided waves from the Pamir seismic zone provide  
 405 additional evidence for the existence of subducted continental lower crust.  
 406 *Tectonophysics*, *762*, 1–16.
- 407 Mechie, J., Yuan, X., Schurr, B., Schneider, F., Sippl, C., Ratschbacher, L., . . . oth-  
 408 ers (2012). Crustal and uppermost mantle velocity structure along a profile  
 409 across the Pamir and southern Tien Shan as derived from project TIPAGE  
 410 wide-angle seismic data. *Geophysical Journal International*, *188*(2), 385–407.
- 411 Metzger, S., Ischuk, A., Deng, Z., Ratschbacher, L., Perry, M., Kufner, S.-K., . . .  
 412 Moreno, M. (2020). Dense GNSS profiles across the northwestern tip of  
 413 the India-Asia collision zone: Triggered slip and westward flow of the Pe-  
 414 ter the First Range, Pamir, into the Tajik Depression. *Tectonics*, *39*(2),  
 415 e2019TC005797.
- 416 Metzger, S., Schurr, B., Ratschbacher, L., Sudhaus, H., Kufner, S.-K., Schöne, T.,  
 417 . . . Bendick, R. (2017). The 2015 Mw7. 2 Sarez Strike-Slip Earthquake in the  
 418 Pamir Interior: Response to the Underthrusting of India’s Western Promon-  
 419 tory. *Tectonics*, *36*(11), 2407–2421.
- 420 Pegler, G., & Das, S. (1998). An enhanced image of the Pamir–Hindu Kush seis-  
 421 mic zone from relocated earthquake hypocentres. *Geophysical Journal Interna-*  
 422 *tional*, *134*(2), 573–595.
- 423 PMP International (Tajikistan). (2005). *Tajikistan National Seismic Network*. Inter-  
 424 national Federation of Digital Seismograph Networks. Retrieved from [http://](http://www.fdsn.org/doi/10.7914/SN/TJ)  
 425 [www.fdsn.org/doi/10.7914/SN/TJ](http://www.fdsn.org/doi/10.7914/SN/TJ) doi: 10.7914/SN/TJ
- 426 Rondenay, S., Abers, G. A., & Van Keken, P. E. (2008). Seismic imaging of subduc-  
 427 tion zone metamorphism. *Geology*, *36*(4), 275–278.

- 428 Schneider, F., Yuan, X., Schurr, B., Mechie, J., Sippl, C., Haberland, C., ... others  
429 (2013). Seismic imaging of subducting continental lower crust beneath the  
430 Pamir. *Earth and Planetary Science Letters*, *375*, 101–112.
- 431 Schneider, F., Yuan, X., Schurr, B., Mechie, J., Sippl, C., Kufner, S.-K., ... others  
432 (2019). The crust in the Pamir: Insights from receiver functions. *Journal of*  
433 *Geophysical Research: Solid Earth*, *124*(8), 9313–9331.
- 434 Schwab, M., Ratschbacher, L., Siebel, W., McWilliams, M., Minaev, V., Lutkov,  
435 V., ... others (2004). Assembly of the Pamirs: Age and origin of magmatic  
436 belts from the southern Tien Shan to the southern Pamirs and their relation to  
437 Tibet. *Tectonics*, *23*(4).
- 438 SEISDMC. (2021). Data management centre of the China National Seismic Net-  
439 work at the Institute of Geophysics. *China Earthquake Administration*. doi: 10  
440 .11998/SeisDmc/SN
- 441 Sippl, C., Schurr, B., Tynpel, J., Angiboust, S., Mechie, J., Yuan, X., ... others  
442 (2013). Deep burial of Asian continental crust beneath the Pamir imaged  
443 with local earthquake tomography. *Earth and Planetary Science Letters*, *384*,  
444 165–177.
- 445 Sippl, C., Schurr, B., Yuan, X., Mechie, J., Schneider, F., Gadoev, M., ... others  
446 (2013). Geometry of the Pamir-Hindu Kush intermediate-depth earthquake  
447 zone from local seismic data. *Journal of Geophysical Research: Solid Earth*,  
448 *118*(4), 1438–1457.
- 449 Sobel, E. R., Chen, J., Schoenbohm, L. M., Thiede, R., Stockli, D. F., Sudo, M., &  
450 Strecker, M. R. (2013). Oceanic-style subduction controls late Cenozoic defor-  
451 mation of the Northern Pamir orogen. *Earth and Planetary Science Letters*,  
452 *363*, 204–218.
- 453 Thurber, C. H. (1983). Earthquake locations and three-dimensional crustal structure  
454 in the Coyote Lake area, central California. *Journal of Geophysical Research:*  
455 *Solid Earth*, *88*(B10), 8226–8236.
- 456 van Hinsbergen, D. J., Lippert, P. C., Li, S., Huang, W., Advokaat, E. L., & Spak-  
457 man, W. (2019). Reconstructing Greater India: Paleogeographic, kinematic,  
458 and geodynamic perspectives. *Tectonophysics*, *760*, 69–94.
- 459 Waldhauser, F., & Ellsworth, W. L. (2000). A double-difference earthquake location  
460 algorithm: Method and application to the northern Hayward fault, California.  
461 *Bulletin of the Seismological Society of America*, *90*(6), 1353–1368.
- 462 Wessel, P., Smith, W. H., Scharroo, R., Luis, J., & Wobbe, F. (2013). Generic map-  
463 ping tools: improved version released. *Eos, Transactions American Geophysical*  
464 *Union*, *94*(45), 409–410.
- 465 Wittlinger, G., Vergne, J., Tapponnier, P., Farra, V., Poupinet, G., Jiang, M., ...  
466 Paul, A. (2004). Teleseismic imaging of subducting lithosphere and Moho  
467 offsets beneath western Tibet. *Earth and Planetary Science Letters*, *221*(1-4),  
468 117–130.
- 469 Xu, Q., Zhao, J., Yuan, X., Liu, H., Ju, C., Schurr, B., & Bloch, W. (2021). Deep  
470 crustal contact between the Pamir and Tarim Basin deduced from receiver  
471 functions. *Geophysical Research Letters*.
- 472 Yuan, X., Schurr, B., Bloch, W., Xu, Q., & Zhao, J. (2018). East Pamir seismic net-  
473 work. *GFZ Data services*. doi: 10.14470/3U7560589977
- 474 Yuan, X., Schurr, B., Kufner, S.-K., & Bloch, W. (2018). Sarez Pamir aftershock  
475 seismic network. *GFZ Data services*. doi: 10.14470/4U7561589984
- 476 Yuan, X., Sobolev, S. V., Kind, R., Oncken, O., Bock, G., Asch, G., ... others  
477 (2000). Subduction and collision processes in the Central Andes constrained by  
478 converted seismic phases. *Nature*, *408*(6815), 958–961.
- 479 Zhao, J., Yuan, X., Liu, H., Kumar, P., Pei, S., Kind, R., ... others (2010). The  
480 boundary between the Indian and Asian tectonic plates below Tibet. *Proceed-*  
481 *ings of the National Academy of Sciences*, *107*(25), 11229–11233.
- 482 Zubovich, A. V., Wang, X.-q., Scherba, Y. G., Schelochkov, G. G., Reilinger, R.,

483

Reigber, C., ... others (2010). GPS velocity field for the Tien Shan and  
484 surrounding regions. *Tectonics*, 29(6).

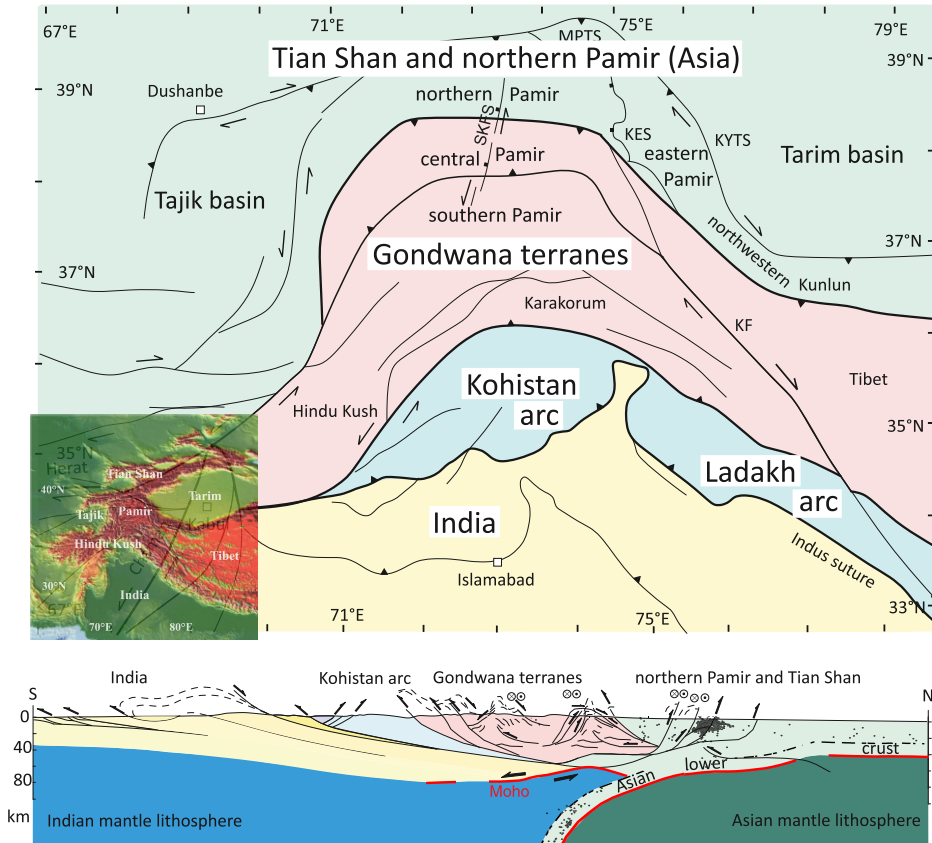


**Figure 1.** Tectonic units of the Pamir in map view and as a schematic cross section along  $\sim 74^\circ\text{E}$ . Deep structure mostly from (Schneider et al., 2013). KES: Kongur Extensional System; KF: Karakorum Fault; KYTS: Kashgar-Yecheng Transfer System; MPTS: Main Pamir Thrust System; SKFS: Sarez-Karakul Fault System

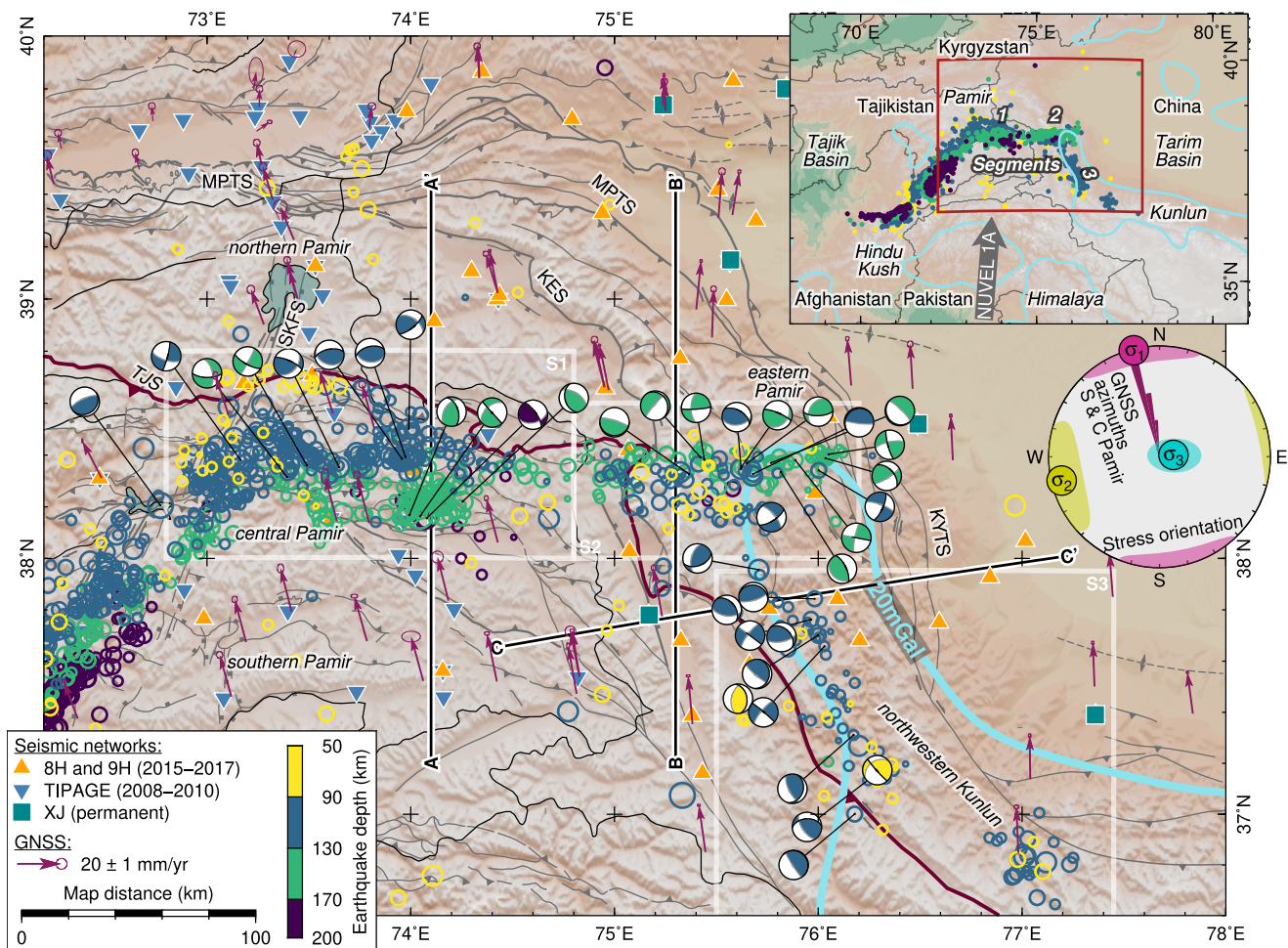


**Figure 2.** Seismotectonic map of the Pamir and northwestern Kunlun with seismic networks, seismicity at intermediate depth, focal mechanisms (black and gray nodal planes indicate fault and auxiliary plane preferred by stress inversion), global navigation satellite system (GNSS) velocity field (Ischuk et al., 2013; Zubovich et al., 2010), and 20mGal positive isostatic gravity anomaly (Balmino et al., 2012). Abbreviations as in Fig. 1. TJS: Tanyamas-Jinsha suture; S1, S2, S3: segments 1 to 3; Map inset: Regional overview. Stereo-net inset: Lower hemisphere stereographic projection of stress directions and 95% confidence ellipsoids (Fig. S15) and histogram of GNSS azimuths in the southern and central Pamir ( $<38.8^\circ\text{N}$ ,  $73\text{--}77^\circ\text{E}$ ,  $5^\circ$  bins)

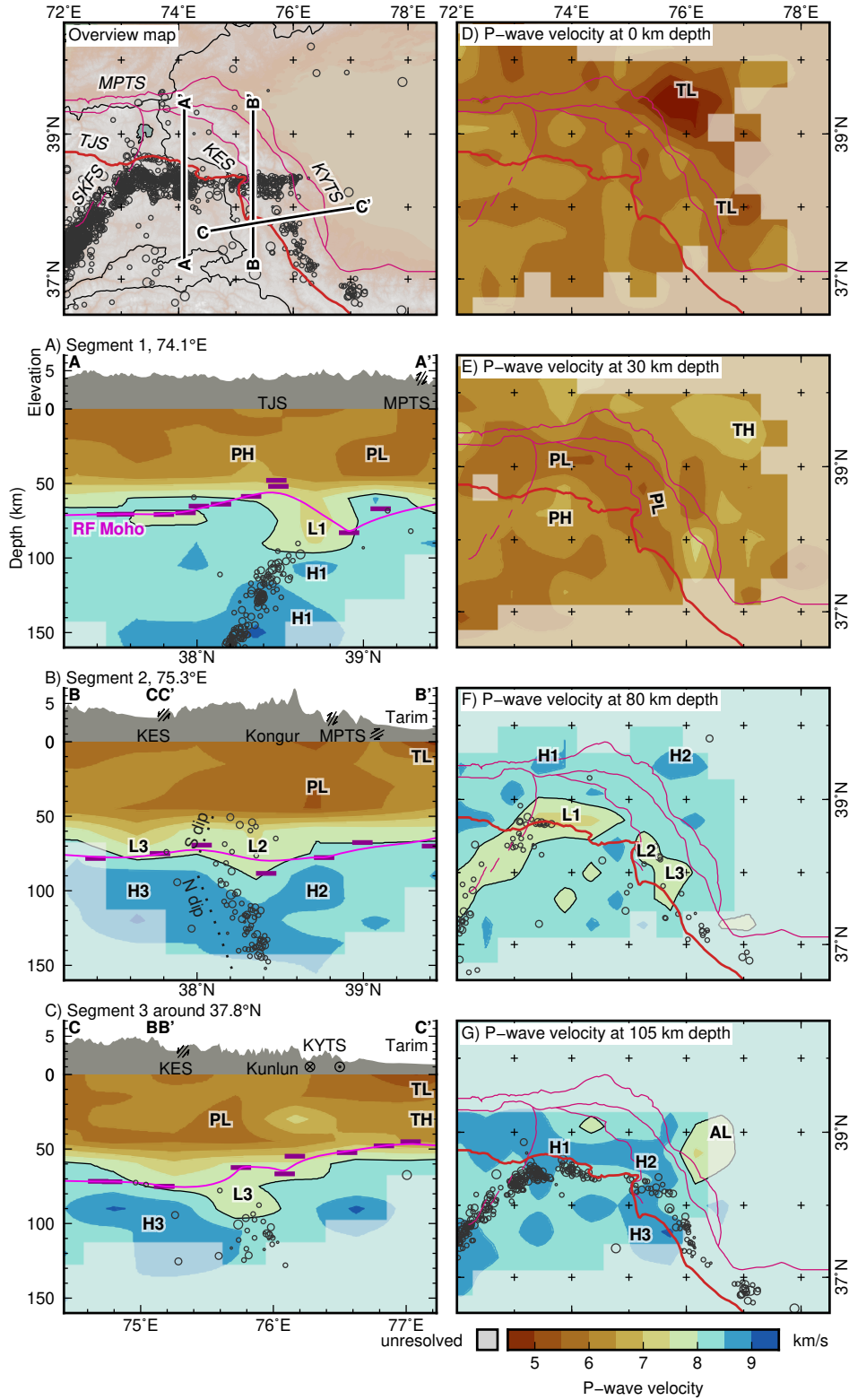


**Figure 3.** Sections through the tomogram. A-C) Profiles shown on overview map; swath width  $\pm 25$  km; no vertical exaggeration in the depth profiles. Dark/light magenta: Receiver function Moho at individual stations and interpolated depth (Schneider et al., 2019; Xu et al., 2021). D-G) Horizontal sections. TH, PH, H1, H2, H3: high velocity zones. TL, PL, L1, L2, L3, AL: low velocity zones.

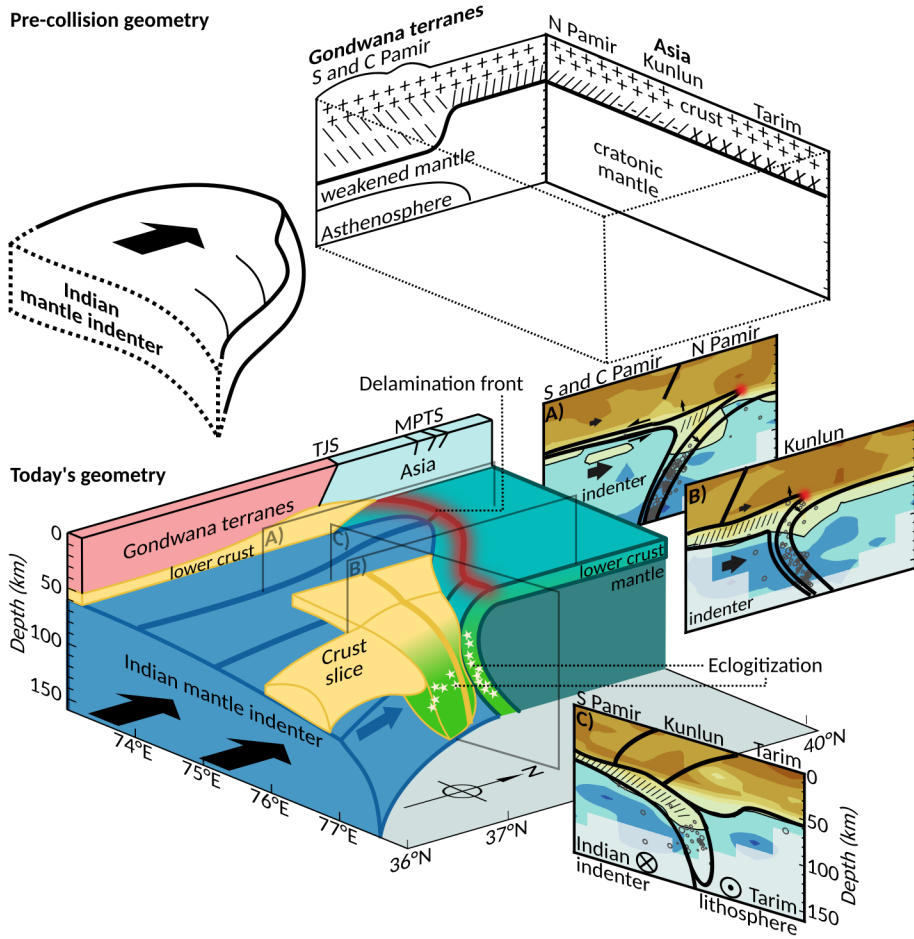


**Figure 4.** Structural interpretation of the P-wave velocity structure, seismicity distribution, and stresses. Top: pre-collision geometry. Bottom: interpreted block diagram of the deep lithospheric structure beneath the Pamir and northwestern Kunlun. A-C) Interpreted cross sections of Fig. 3. '////' symbols mark the lower crust involved in the collision process.

1 **Supporting Information for "Structure and stress**  
2 **field of the lithosphere between Pamir and Tarim"**

Wasja Bloch<sup>1</sup>, Bernd Schurr<sup>1</sup>, Xiaohui Yuan<sup>1</sup>, Lothar Ratschbacher<sup>2</sup>,

Sanaa Reuter<sup>2</sup>, Sofia-Katerina Kufner<sup>1,3</sup>, Qiang Xu<sup>4,5</sup>, Junmeng Zhao<sup>4,5</sup>

3 <sup>1</sup>GFZ German Research Centre for Geosciences, 14473 Potsdam, Germany

4 <sup>2</sup>Geologie, Technische Universität Bergakademie Freiberg, 09599 Freiberg, Germany

5 <sup>3</sup>British Antarctic Survey, Cambridge CB3 0ET, England

6 <sup>4</sup>Key Laboratory of Continental Collision and Plateau Uplift, Institute of Tibetan Plateau Research, Chinese Academy of Sciences,

7 Beijing 100101, China

8 <sup>5</sup>CAS Center for Excellence in Tibetan Plateau Earth Sciences, Beijing 100101, China

9 **Contents of this file**

10 1. Text S1 to Text S5

11 2. Figure S1 to Figure S16

12 **Additional Supporting Information (Files uploaded separately)**

13 1. Captions for Datasets S1 to S3

---

Corresponding author: Wasja Bloch (wbloch@eoas.ubc.ca). Now at: Earth, Ocean and Atmospheric Sciences, University of British Columbia, Vancouver, Canada.



14 **Introduction** This supporting information gives details of the processing steps briefly  
15 described in the main article. Additional figures, allowing to understand seismic network  
16 sensitivity, as well as performance and stability of the 3-dimensional velocity model, are  
17 presented. The seismic event catalog, earthquake focal mechanism catalog, and seismic  
18 wave speed model, are published as separate data files and briefly described here.

19 **Text S1. Data** We operated the East Pamir seismic network (FDSN code 8H; Yuan,  
20 Schurr, Bloch, et al., 2018) with 30 sites in the eastern Pamir, northwestern Kunlun,  
21 and northwestern Tarim basin between August 2015 and July 2017, and the Sarez-Pamir  
22 aftershock seismic network (FDSN code 9H Yuan, Schurr, Kufner, & Bloch, 2018) with  
23 10 sites in the central Pamir between February 2016 and July 2017. We used additional  
24 seismic waveform data from the Xinjiang regional seismic network (XJ; SEISDMC, 2021)  
25 and the Tajik National Seismic Network (FDSN network code TJ; SEISDMC, 2021).

### 26 **Text S2. Seismic Event Detection, Phase Picking, and Initial Localization**

27 We detected 39,309 seismic events, 10,900 of which at intermediate depth ( $>50$  km),  
28 using the *Lassie* earthquake detector (Comino et al., 2017). We computed the moveout  
29 of smoothed, pulse-like image functions of the seismograms and stacked them for trial  
30 subsurface points on a rectangular grid of  $100 \times 100 \times 10$  with a spacing of  $10 \times 10 \times 30$  km  
31 using the 1-D velocity model of (Sippl, Schurr, Yuan, et al., 2013). Peaks from coherent  
32 stacking of the image functions indicated the detection of a seismic event and an initial  
33 location and predicted P- and S-wave arrival times were used as a starting point for phase  
34 picking.

35 We automatically picked P-wave arrival times with *MannekenPix* (Aldersons, 2004),  
36 where initial picks from *obspy*'s STA/LTA trigger and predicted picks from the detection  
37 routine were used as starting points; S-wave arrival times were picked with *spicker* (Diehl  
38 et al., 2009). Filter window lengths and positions for both pickers were calibrated from  
39 a set of 59 manually picked phase arrivals. After each arrival time picking run, events  
40 were located with *hypo71* (Lee & Lahr, 1972), and picks with the highest residuals were

41 removed subsequently until the location root-mean-square misfit fell below a threshold of  
42 2 s for P-waves only and 3 s for P- and S-waves combined. We then used a subset of 1,855  
43 seismic events with the best constrained arrival-time picks to invert for a depth-dependent  
44 1-D velocity model and static station corrections using *veltest* (Kissling et al., 1994). We  
45 again relocated all events in this model and removed those arrival times that yielded a  
46 residual 5 times larger than the standard deviation of all residuals of a certain seismic  
47 phase on a certain station. In total, we located 29,795 seismic events in the crust and  
48 mantle this way.

### 49 **Text S3. Inversion for the Subsurface Velocity Field**

50 To derive a dataset suitable for tomographic inversion, we augmented the catalog with  
51 events from Sippl, Schurr, Tympel, et al. (2013) and used a spatially declustered set of  
52 2,264 events from the combined catalog with a total of 38,423 well-constrained P- and  
53 15,910 S-arrival times. Inversion for the 3-D subsurface P-wave velocity structure was  
54 conducted using *simulps* (Thurber, 1983).

55 The seismic velocity field was parameterized as gradients between a rectangular grid of  
56 nodes. After testing of various node configurations, we used a node spacing of 40 km in  
57 horizontal and 15 km in vertical direction (Figs. S1a and S2). The 1-D starting model was  
58 found by first inverting for the 1-D velocity gradients between vertical nodes and station  
59 corrections. Then, we constrained the velocities to increase with depth and that they  
60 do not exceed the velocity at 75-km depth (Fig. S1a). The model space was explored  
61 with various damping parameters applied in the inversions (Fig. S1b). The final model  
62 was found by first inverting solely for the velocity structure and earthquake parameters,

63 and then allowing for minor adjustments by letting non-modeled residuals be taken up by  
64 station corrections. The nodes of the input velocity model were modified with alternating  
65 anomalies of  $\pm 5\%$  in a checkerboard resolution test that was used to assess the sensitivity  
66 of the model and as guidance to mask poorly resolved regions (Fig. S2 to S5).

67 We assessed the presence of smearing artifacts by computing synthetic travel times  
68 in our derived velocity model, inverting them again for the velocity structure from the  
69 original starting model and plotting the ray paths (Fig. S6 to S9).

70 We performed recovery tests for the anomalies that are most important to our inter-  
71 pretation by increasing (decreasing) the velocity of the 1D starting model by 0.5 km/s  
72 at the location of the interpreted high (low) velocity zones, computing synthetic travel  
73 times for this data set and adding random Gaussian noise with a standard deviation of  
74 0.05, 0.1, 0.2, or 0.4 s for pick classes 0, 1, 2, and 3. We then tried to recover the found  
75 velocity structure with the inversion strategy described above. The results are plotted in  
76 Fig. S10); they indicate the velocity anomalies *L3*, *H3*, *L1*, *PH*, and *PL* are adequately  
77 imaged by the inversion routine.

#### 78 **Text S4. Location uncertainty and relative event relocation**

79 To focus on sub-crustal processes, we disregarded crustal earthquakes (<50-km depth),  
80 which were dominated by a strong earthquake sequence and are confined to the upper  
81  $\sim 40$ -km depth. We added intermediate-depth earthquakes to our seismicity catalog with  
82 at least 4 S-picks, which were previously excluded in the tomographic inversion. We then  
83 relocated all events with in the derived 3-D velocity model. To get a conservative estimate  
84 of the location uncertainty, we regridded the 3-D gradient model on a 5 km grid, localized

85 the events with *NonLinLoc* (Lomax et al., 2000) in the 3-D model, and report 2 times  
86 the square root of the diagonal elements of the covariance matrix as the 95% confidence  
87 intervals in longitude, latitude, and depth direction (Fig. S13). To assess the influence of  
88 the 3-D model on locations and location uncertainties, we also located the events in the  
89 1D model of Sippl, Schurr, Yuan, et al. (2013) (Fig. S12).

90 We then relocated all events using the *hypoDD* algorithm (Waldhauser & Ellsworth,  
91 2000), using differential P- and S-wave catalog arrival times.

## 92 **Text S5. Focal Mechanisms and Stress Directions**

93 For 29 events, we observed P-wave first motion polarities and Cartesian P-to-S ampli-  
94 tude ratios on the 1 Hz highpass filtered seismograms and projected them to the focal  
95 sphere using the velocity model of Sippl, Schurr, Yuan, et al. (2013) using the workflow of  
96 Bloch, Schurr, Kummerow, Salazar, and Shapiro (2018). We then inverted for the earth-  
97 quake focal mechanism using the *HASH* algorithm (Hardebeck & Shearer, 2003; Bloch et  
98 al., 2018), and added 9 moment tensors of Kufner et al. (2016).

99 We used all focal mechanisms to invert for the deviatoric unit stress tensor by minimiz-  
100 ing the misorientation between the earthquake slip vector and the predicted tangential  
101 traction on the fault plane. To resolve the nodal plane ambiguity, we first searched all  
102 stress tensors in angle intervals of  $2^\circ$  and shape factor intervals of 0.1 for the one that  
103 results in the lowest combined misfit, and selected the nodal planes with the lower mis-  
104 orientation as fault planes (Gephart & Forsyth, 1984). We then inverted for the principal  
105 stress directions using the *slick* algorithm and evaluated the uncertainty in the orientation  
106 using a bootstrapping approach (Fig. S15 Michael, 1987, 1984). We tested the stability

107 of the found solutions by performing the inversion also separately for the three seismicity  
108 segments discussed in the main article (Fig. S15)

109 **Data Set S1.**

110 Bloch\_et-al\_2021\_GRL\_seismic\_event\_catalog.txt

111 The seismic event catalog presented in the main article.

112 Seismic events from years 2008-2010 are relocated from Sippl, Schurr, Tymphel, et al.

113 (2013)

114 Columns are:

- 115 • Year, Month, Day, Hour, Minute, Second: Time of the seismic event
- 116 • Timestamp: Time of the event in seconds since 1. January 1970
- 117 • Longitude, Latitude: Coordinated of the event location in degree
- 118 • Depth: Depth of the event in kilometer
- 119 • sigEW, sigNS, sigZ: 95% confidence limits of the event location in latitudinal, longi-  
120 tudinal, and depth direction.
- 121 • Magnitude: Local magnitude of the seismic event
- 122 • P-picks, S-picks: Number of P- and S-wave arrival times used for event location
- 123 • method: Localization algorithm that yielded the reported location

124 **Data Set S2.** Bloch\_et\_al\_2021\_GRL\_focal\_mechanism\_catalog.txt Columns are (com-

125 patible with *Generic Mapping Tools psmeca -Sa*):

- 126 1. Longitude of the event location in degree
- 127 2. Latitude of the event location in degree
- 128 3. Depth of the event in kilometer
- 129 4. Strike of the preferred fault plane in degree clockwise from north
- 130 5. Dip of the preferred fault plane in degree down from horizontal

- 131 6. Rake of the slip vector on the fault plane in degree clockwise from strike direction
- 132 7. Local magnitude of the event
- 133 8. Unused placeholder
- 134 9. Unused placeholder
- 135 10. Time of the event (UTC)

136 Last 9 rows are from Kufner et al. (2016).

### 137 **Data Set S3.**

138 velocity\_model.zip

139 Folder containing the nodes of the tomographic velocity model and scripts to extract  
140 and plot the published and custom profiles.

### References

- 141 Aldersons, F. (2004). Toward three-dimensional crustal structure of the Dead Sea region  
142 from local earthquake tomography. *PhD thesis*.
- 143 Bloch, W., Schurr, B., Kummerow, J., Salazar, P., & Shapiro, S. A. (2018). From slab  
144 coupling to slab pull: Stress segmentation in the subducting Nazca plate. *Geophysical  
145 Research Letters*, *45*(11), 5407–5416.
- 146 Comino, J. Á. L., Heimann, S., Cesca, S., Milkereit, C., Dahm, T., & Zang, A. (2017).  
147 Automated full waveform detection and location algorithm of acoustic emissions from  
148 hydraulic fracturing experiment. *Procedia engineering*, *191*, 697–702.
- 149 Diehl, T., Deichmann, N., Kissling, E., & Husen, S. (2009). Automatic S-wave picker  
150 for local earthquake tomography. *Bulletin of the Seismological Society of America*,  
151 *99*(3), 1906–1920.



- 152 Gephart, J. W., & Forsyth, D. W. (1984). An improved method for determining the  
153 regional stress tensor using earthquake focal mechanism data: application to the  
154 San Fernando earthquake sequence. *Journal of Geophysical Research: Solid Earth*,  
155 *89*(B11), 9305–9320.
- 156 Hardebeck, J. L., & Shearer, P. M. (2003). Using S/P amplitude ratios to constrain  
157 the focal mechanisms of small earthquakes. *Bulletin of the Seismological Society of*  
158 *America*, *93*(6), 2434–2444.
- 159 Kissling, E., Ellsworth, W., Eberhart-Phillips, D., & Kradolfer, U. (1994). Initial refer-  
160 ence models in local earthquake tomography. *Journal of Geophysical Research: Solid*  
161 *Earth*, *99*(B10), 19635–19646.
- 162 Kufner, S.-K., Schurr, B., Sippl, C., Yuan, X., Ratschbacher, L., Ischuk, A., . . . others  
163 (2016). Deep India meets deep Asia: Lithospheric indentation, delamination and  
164 break-off under Pamir and Hindu Kush (Central Asia). *Earth and Planetary Science*  
165 *Letters*, *435*, 171–184.
- 166 Lee, W. H. K., & Lahr, J. C. (1972). *HYP071: A computer program for determining*  
167 *hypocenter, magnitude, and first motion pattern of local earthquakes*. US Department  
168 of the Interior, Geological Survey, National Center for . . . .
- 169 Lomax, A., Virieux, J., Volant, P., & Berge-Thierry, C. (2000). Probabilistic earthquake  
170 location in 3D and layered models. In *Advances in seismic event location* (pp. 101–  
171 134). Springer.
- 172 Michael, A. J. (1984). Determination of stress from slip data: faults and folds. *Journal*  
173 *of Geophysical Research: Solid Earth*, *89*(B13), 11517–11526.

- 174 Michael, A. J. (1987). Use of focal mechanisms to determine stress: a control study.  
175 *Journal of Geophysical Research: Solid Earth*, *92*(B1), 357–368.
- 176 SEISDMC. (2021). Data management centre of the China National Seismic Network  
177 at the Institute of Geophysics. *China Earthquake Administration*. doi: 10.11998/  
178 SeisDmc/SN
- 179 Sippl, C., Schurr, B., Tympel, J., Angiboust, S., Mechie, J., Yuan, X., . . . others (2013).  
180 Deep burial of Asian continental crust beneath the Pamir imaged with local earth-  
181 quake tomography. *Earth and Planetary Science Letters*, *384*, 165–177.
- 182 Sippl, C., Schurr, B., Yuan, X., Mechie, J., Schneider, F., Gadoev, M., . . . others (2013).  
183 Geometry of the Pamir-Hindu Kush intermediate-depth earthquake zone from local  
184 seismic data. *Journal of Geophysical Research: Solid Earth*, *118*(4), 1438–1457.
- 185 Thurber, C. H. (1983). Earthquake locations and three-dimensional crustal structure  
186 in the Coyote Lake area, central California. *Journal of Geophysical Research: Solid*  
187 *Earth*, *88*(B10), 8226–8236.
- 188 Waldhauser, F., & Ellsworth, W. L. (2000). A double-difference earthquake location al-  
189 gorithm: Method and application to the northern Hayward fault, California. *Bulletin*  
190 *of the Seismological Society of America*, *90*(6), 1353–1368.
- 191 Xu, Q., Zhao, J., Yuan, X., Liu, H., Ju, C., Schurr, B., & Bloch, W. (2021). Deep  
192 crustal contact between the Pamir and Tarim Basin deduced from receiver functions.  
193 *Geophysical Research Letters*.
- 194 Yuan, X., Schurr, B., Bloch, W., Xu, Q., & Zhao, J. (2018). East Pamir seismic network.  
195 *GFZ Data services*. doi: 10.14470/3U7560589977

196 Yuan, X., Schurr, B., Kufner, S.-K., & Bloch, W. (2018). Sarez Pamir aftershock seismic  
197 network. *GFZ Data services*. doi: 10.14470/4U7561589984

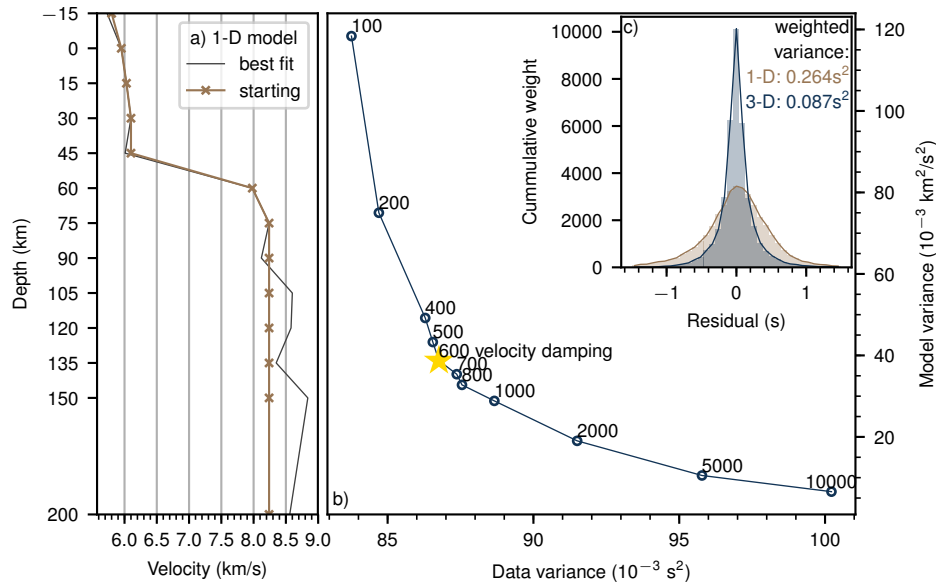


**Figure S1.** a) 1-D models. Best fit: Minimum misfit model after 1-D inversion with *simulps* with station corrections. Starting: Starting model for the 3-D inversion. We applied a positivity and a maximum velocity constraint to avoid pre-defining essential structures in the 3-D inversion b) L-curve to find optimal velocity damping parameter. Star: chosen value c) Reduction of arrival time residuals and variance from 1-D starting model to the presented 3-D model.

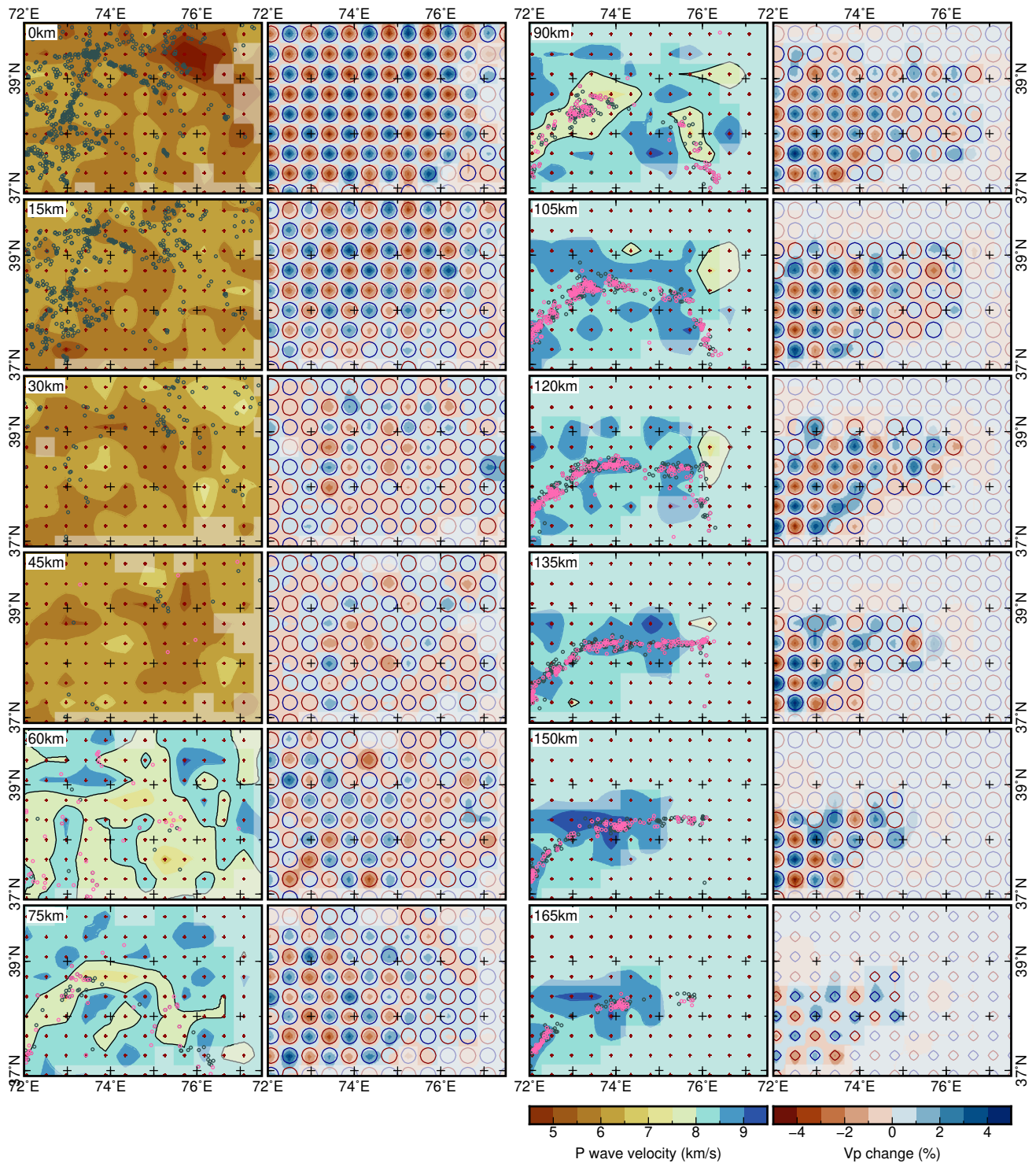


**Figure S2.** Horizontal slices through the tomogram at the node planes. Columns 1 and 3: Seismic velocities (colored background), grid nodes (red crosses), earthquakes used for tomographic inversion (gray circles), relocated earthquakes at intermediate depth (pink circles). Columns 2 and 4: Results of checkerboard recovery test: recovered model (colored background), input model ( $\pm 1\%$  contours, maximum amplitude  $\pm 5\%$ ).

July 20, 2021 3:18pm

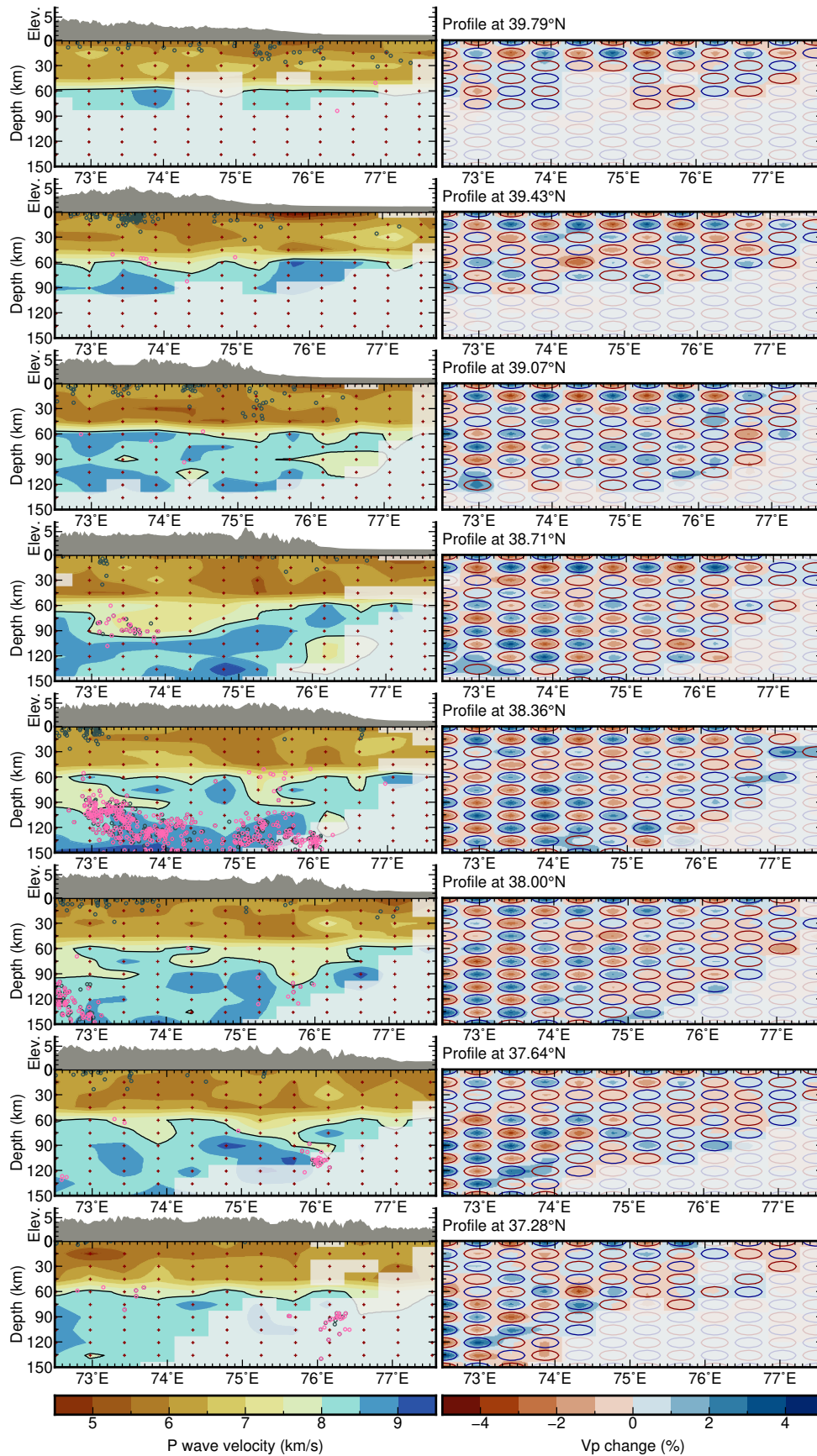
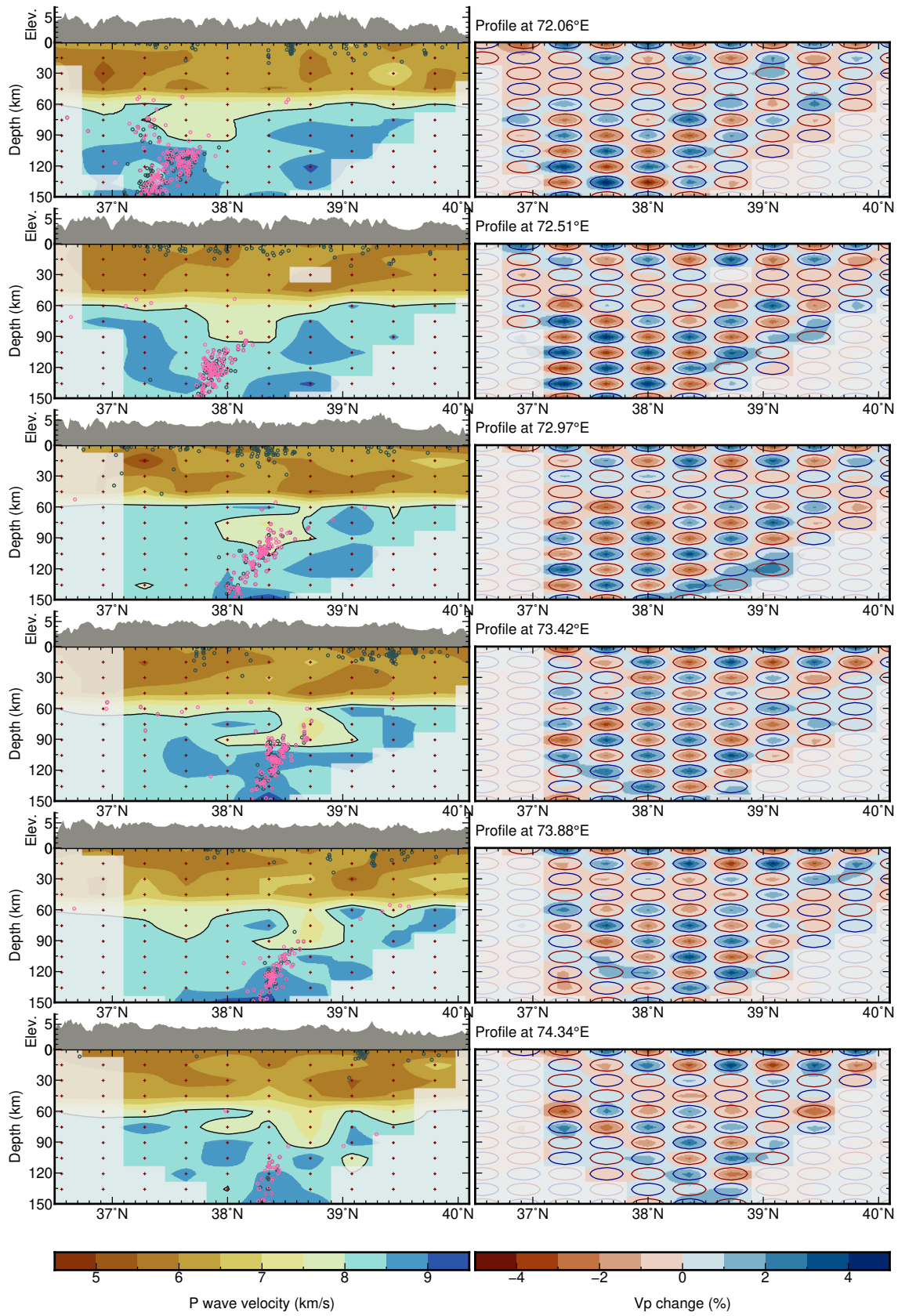


Figure S3. Same as Fig. S3, but with west-east-profiles. July 20, 2021, 3:18pm



**Figure S4.** Same as Fig. S3, but with south-north-profiles.

July 20, 2021, 3:18pm

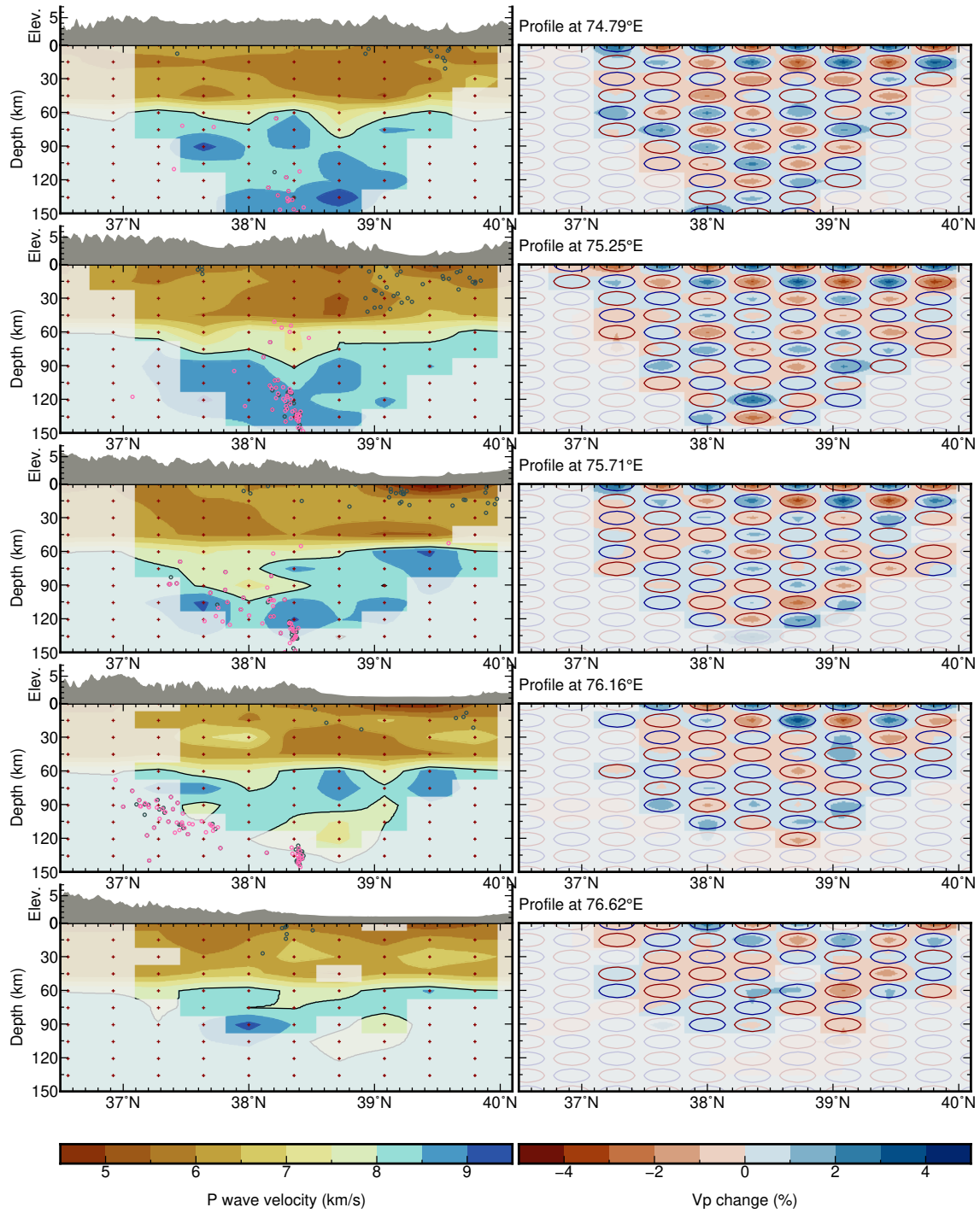
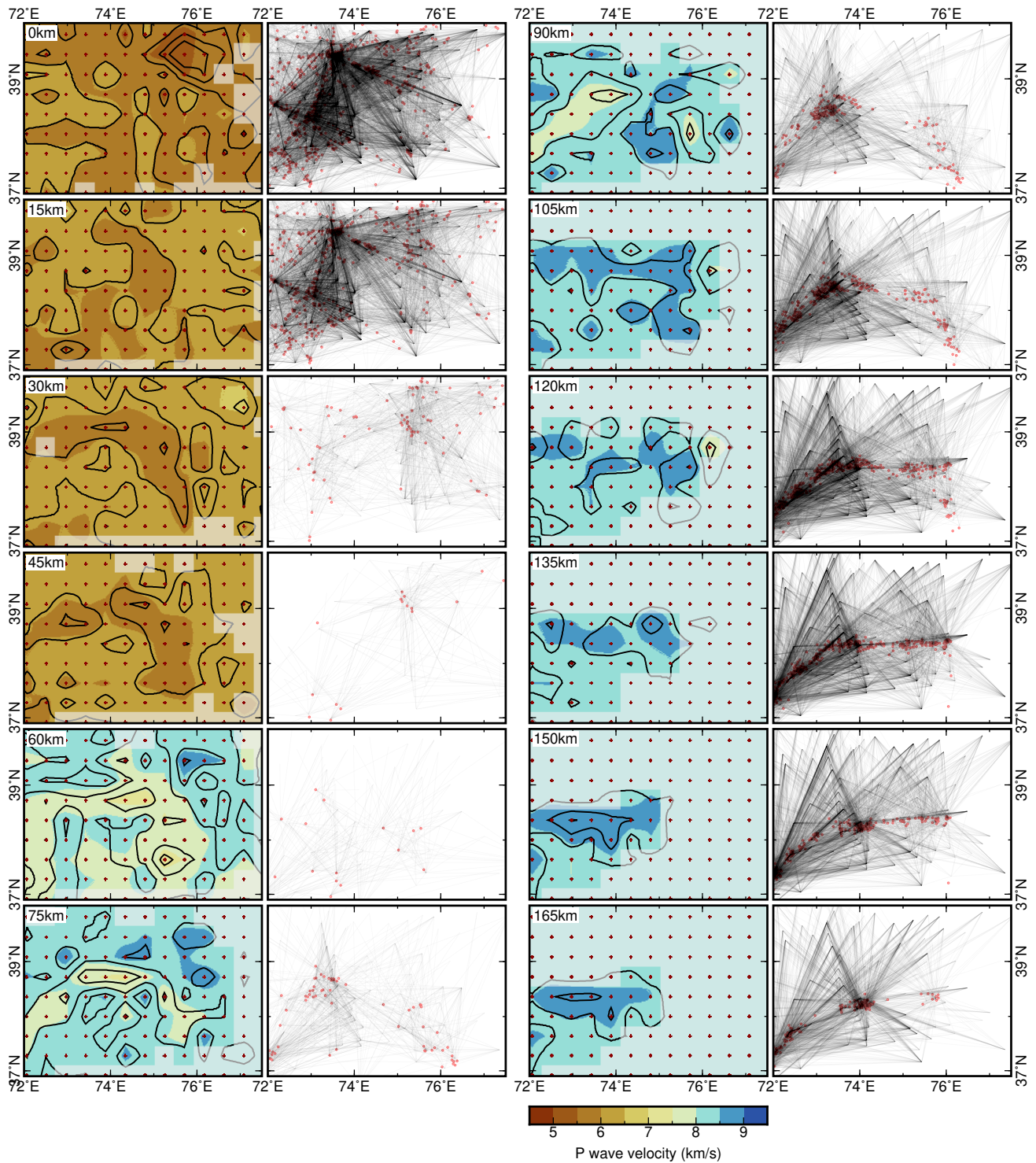


Figure S5. Fig. S4, continued





**Figure S6.** Horizontal slices at the node planes through recovery test of the tomographic inversion. Columns 1 and 3: Input model as in Fig. S2 (contours), and recovered model (colored background). Columns 2 and 4: Ray paths departing in the respective horizontal slice.

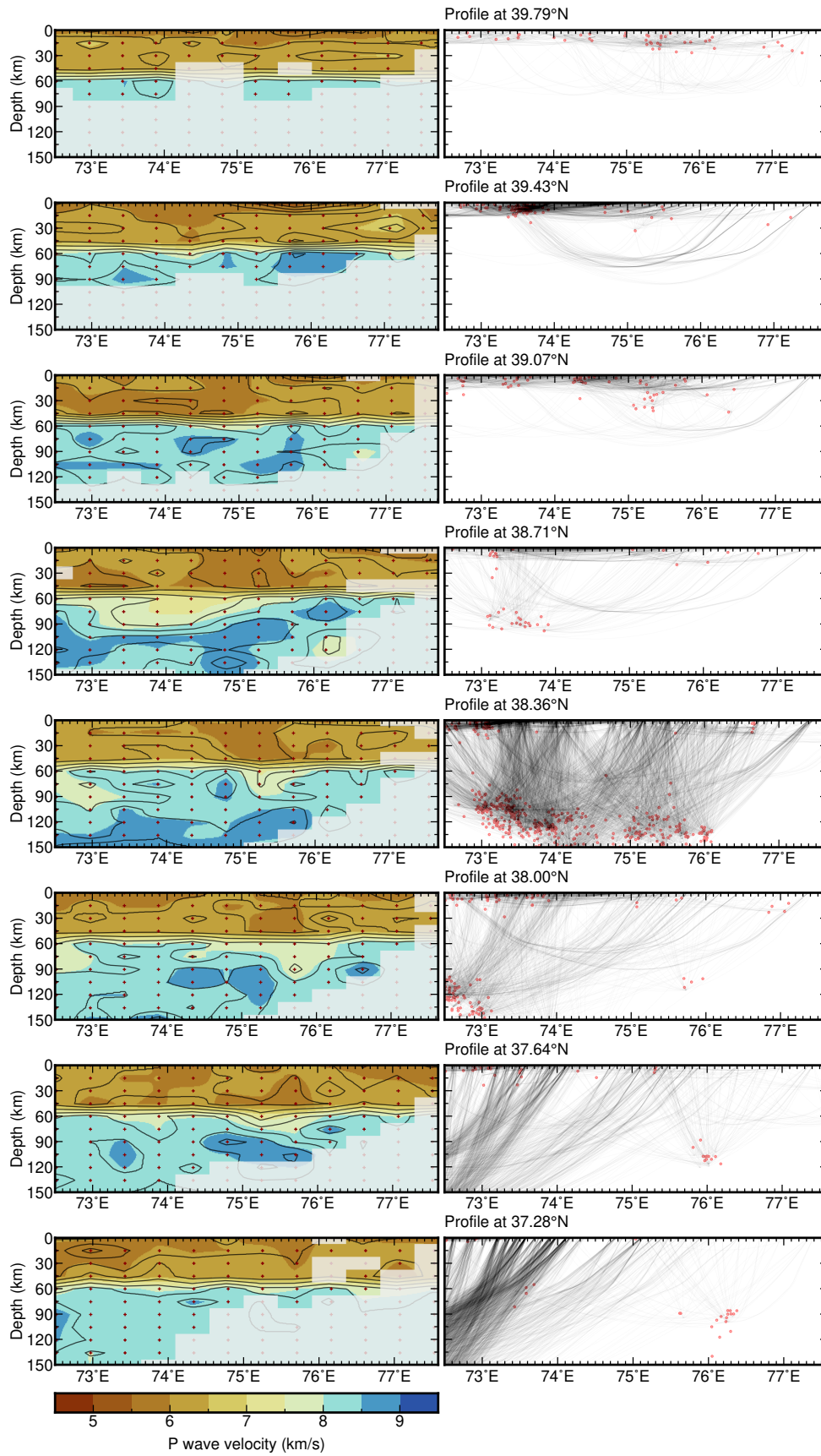
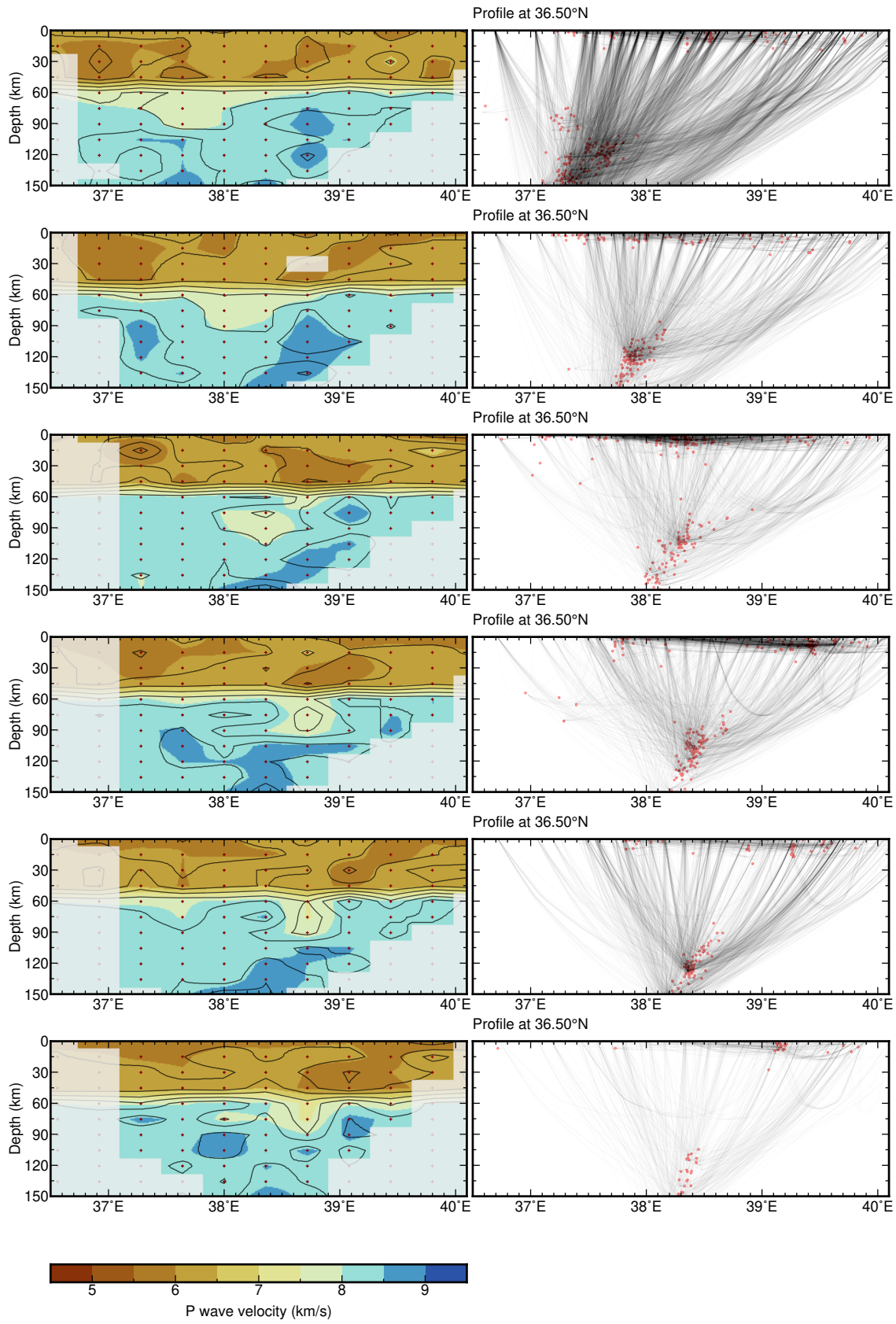


Figure S7. Same as Fig. S6, but with west-east profiles. July 20, 2021, 3:18pm



**Figure S8.** Same as Fig. S7, but with south-north-profiles.  
July 20, 2021, 3:18pm

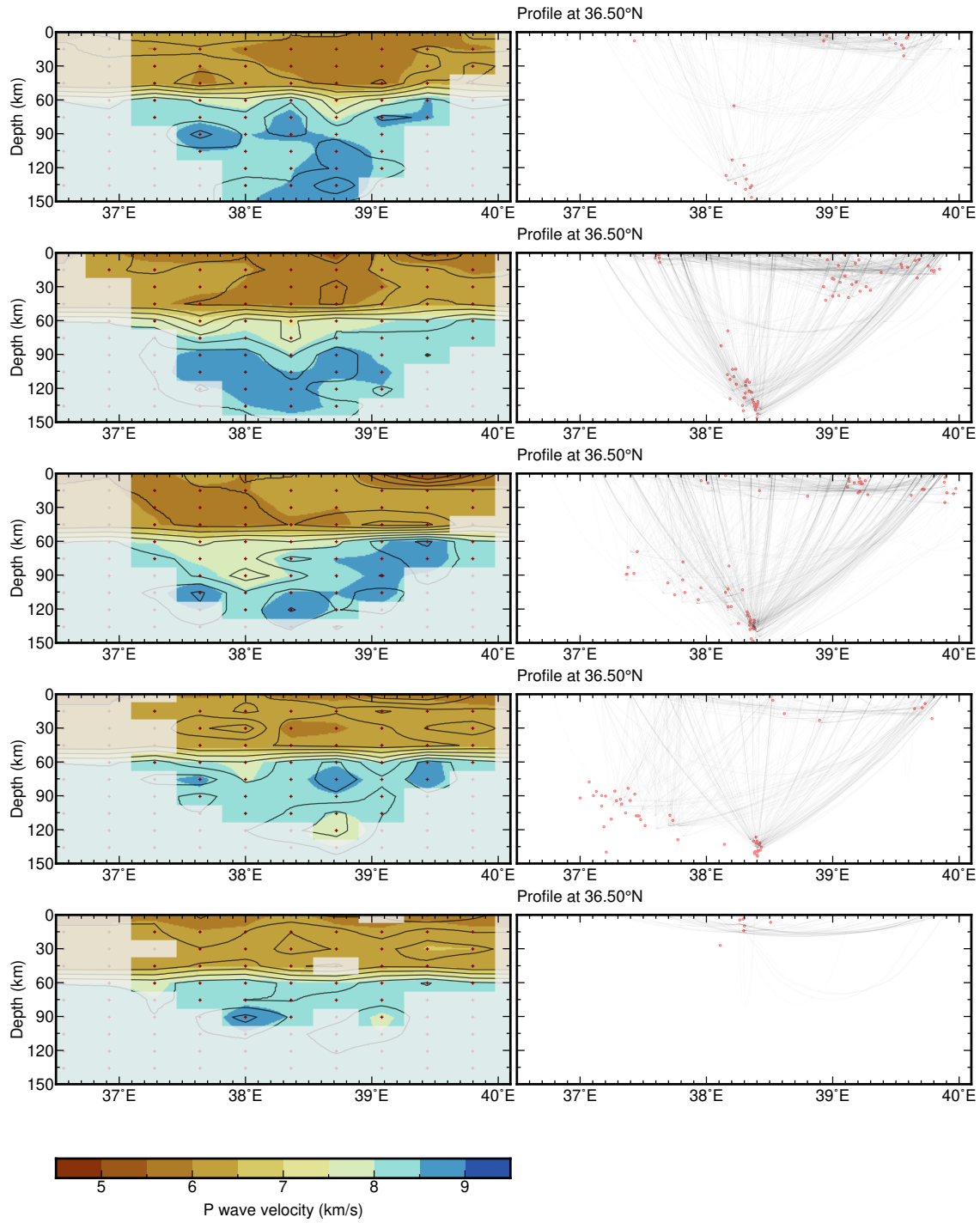
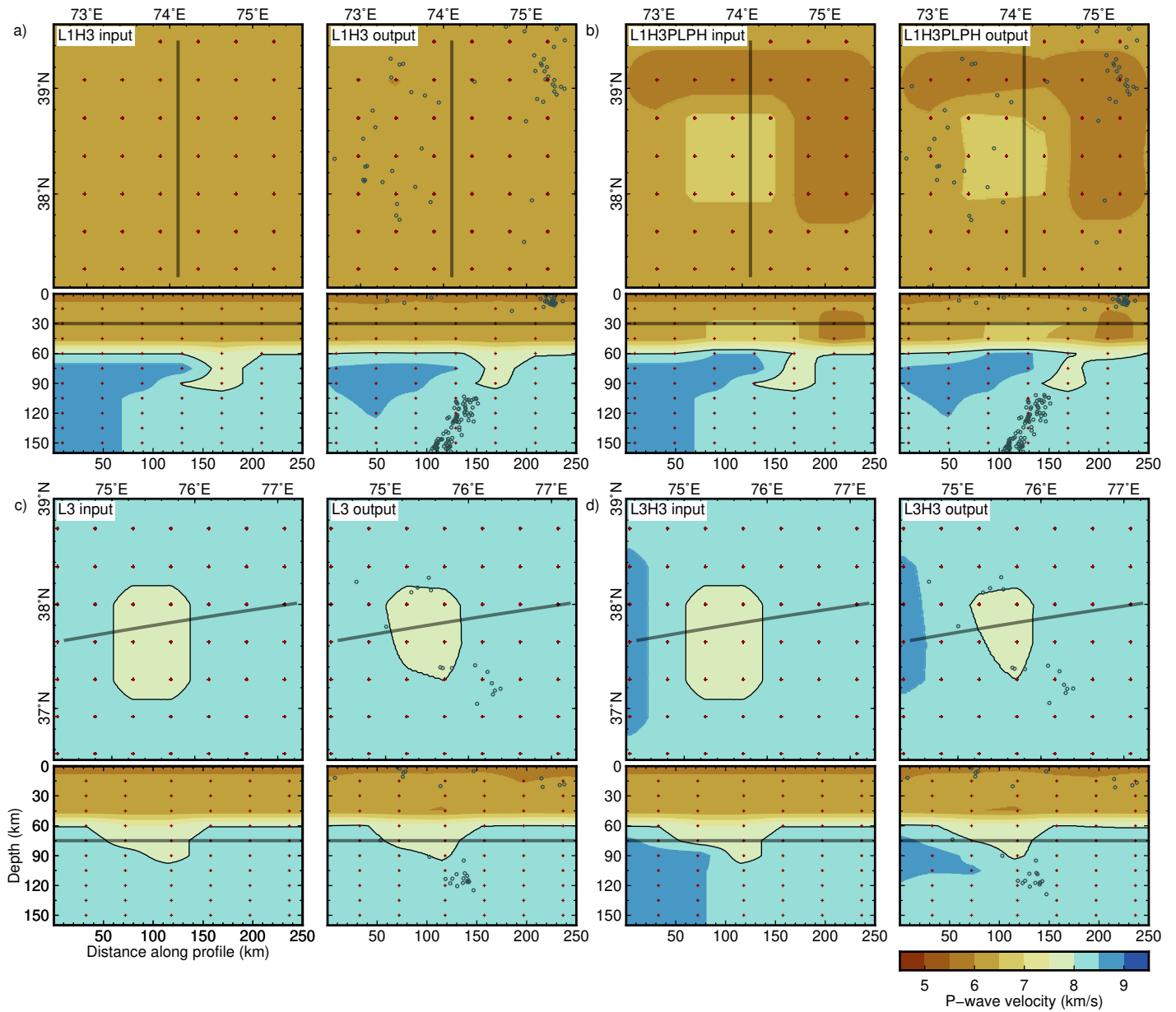
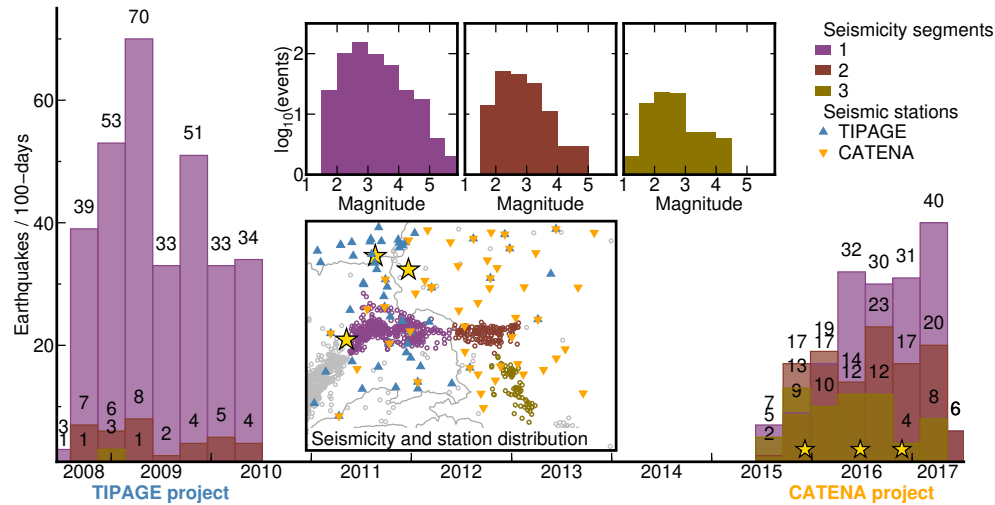


Figure S9. Fig. S8, continued



**Figure S10.** Summary of recovery tests for selected anomalies as close-ups of horizontal slices (top sub-panels) and profiles (bottom sub-panels) through the anomalies, as in Fig. 3 of the main text. Slice depth and profile location indicated as gray lines. Left subfigures: input anomalies. Right subfigures: recovered anomalies. (a) Anomalies *L1* and *H3*. (b) Anomalies *L1*, *H3*, *PL*, and *PH*. (c) Anomaly *L3* only. (d) Anomalies *L3* and *H3*.



**Figure S11.** Seismicity rate, local event magnitudes, and station distribution for the three seismicity segments discussed in the main article. Stations of the TIPAGE project (2008-2010, blue) were located in the Tajik Pamir and covered the central segment. Stations of the CATENA project (2015-2017, orange), including networks 8H, 9H and XJ, were located in the Chinese Pamir and Tarim basin and covered segment 2 and 3. Additional stations were placed in the Tajik Pamir in February 2016. Aftershock sequences of strong earthquakes (stars) in December 2015, June 2016, and November 2016 represent seismic noise that lowered the detection capability of intermediate depth seismicity. Magnitudes of events that occur outside one of the networks (especially in segment 3) tend to be overestimated. Event rate in segment 1 is significantly higher compared to segment 2 and segment 3, despite the different network configuration and noise conditions.

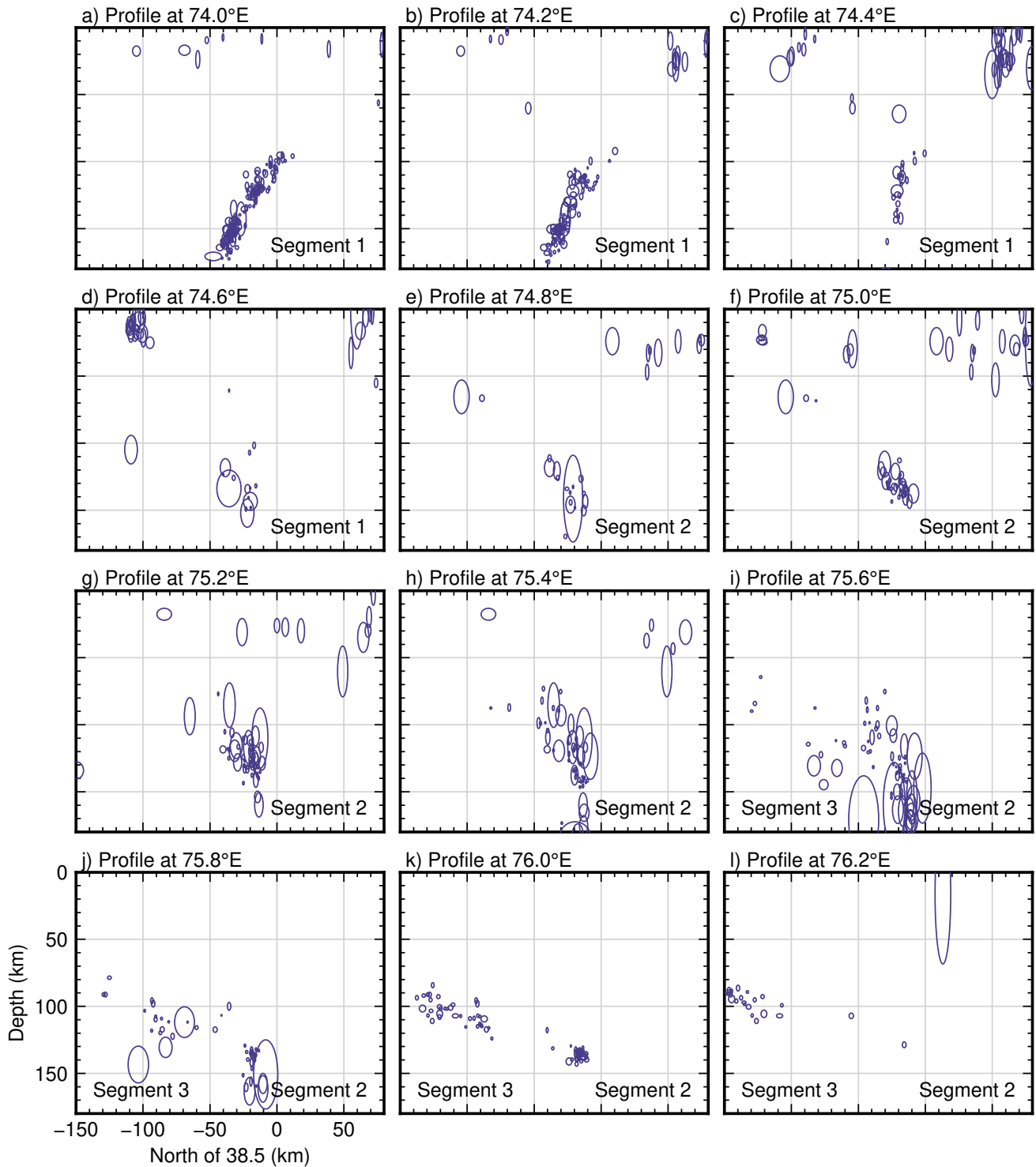


**Figure S12.** North-south seismicity profiles across segments 1 and 2, oblique to segment 3, ellipses indicating 95% location confidence. Profile width  $0.2^\circ$ . Seismicity located in 1D velocity model of Sippl, Schurr, Yuan, et al. (2013).

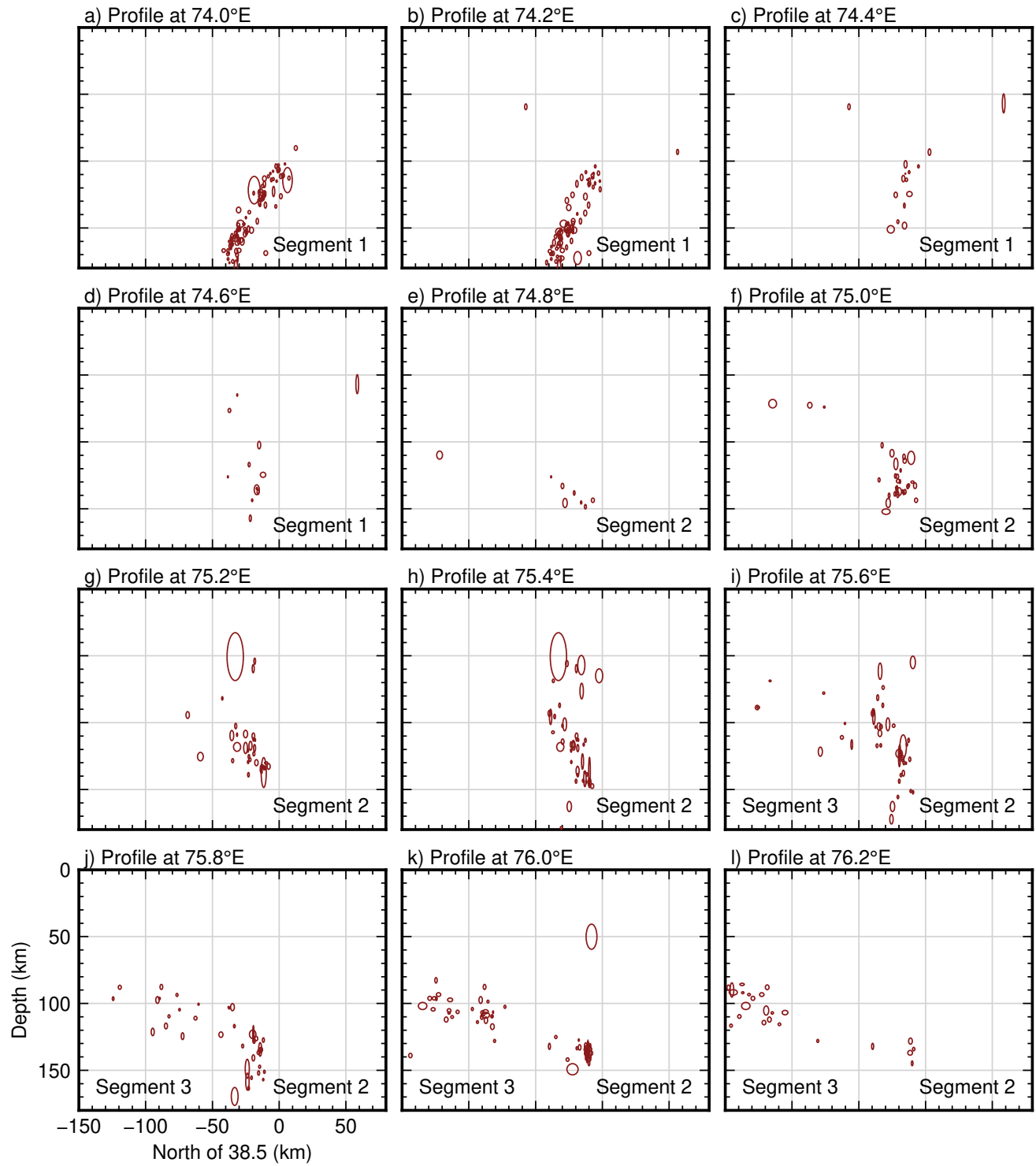


**Figure S13.** As Fig. S13, but only intermediate-depth seismicity (>50 km) relocated in the present 3-D velocity, and adjusted relative locations.



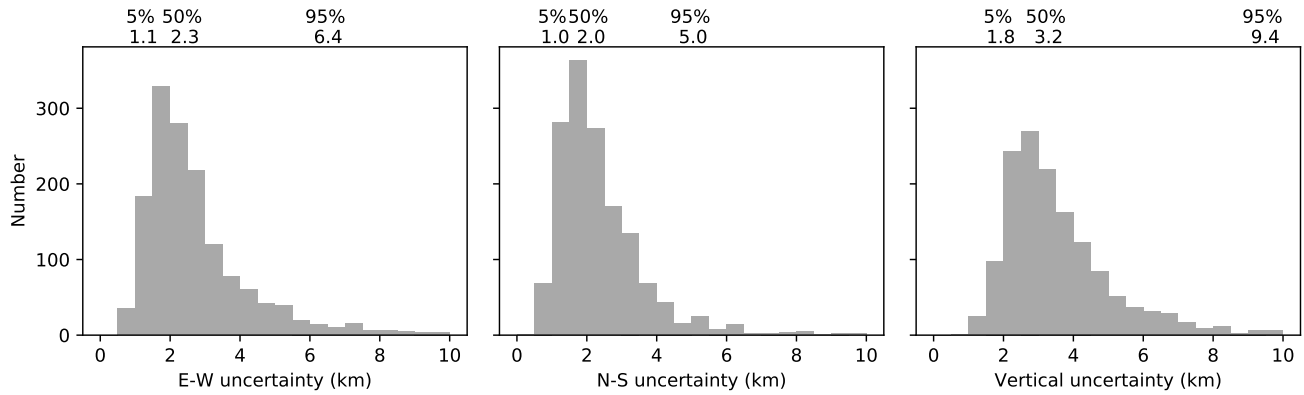


**Figure S14.** Location uncertainties of earthquakes at intermediate depth in east–west, north–south and vertical direction. Top row indicates 5%, 50% (median), and 95% quantiles.

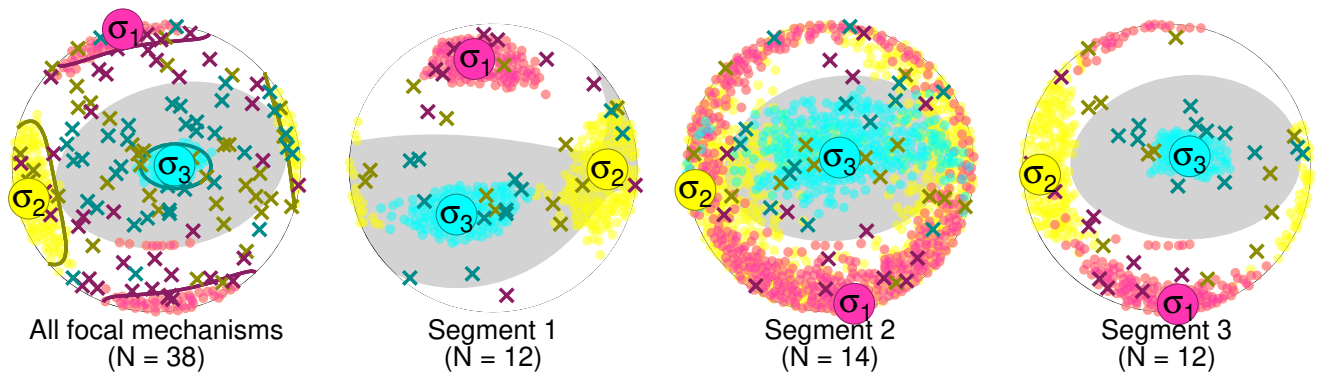


**Figure S15.** Results of stress tensor inversion for (left) all focal mechanisms, as in Fig. 2 of the main text, and (second left to right) clustered subsets of the respective segments. All lower hemisphere stereographic projections. Crosses mark input P- (magenta), N- (yellow), and T-axes (cyan).  $\sigma_1$ ,  $\sigma_2$ , and  $\sigma_3$  are largest, intermediate and smallest principal stress. Transparent dots mark the 95% confidence intervals determined by bootstrapping. Gray shaded background represents positive regions of the stress tensor, white negative. N: number of observations.

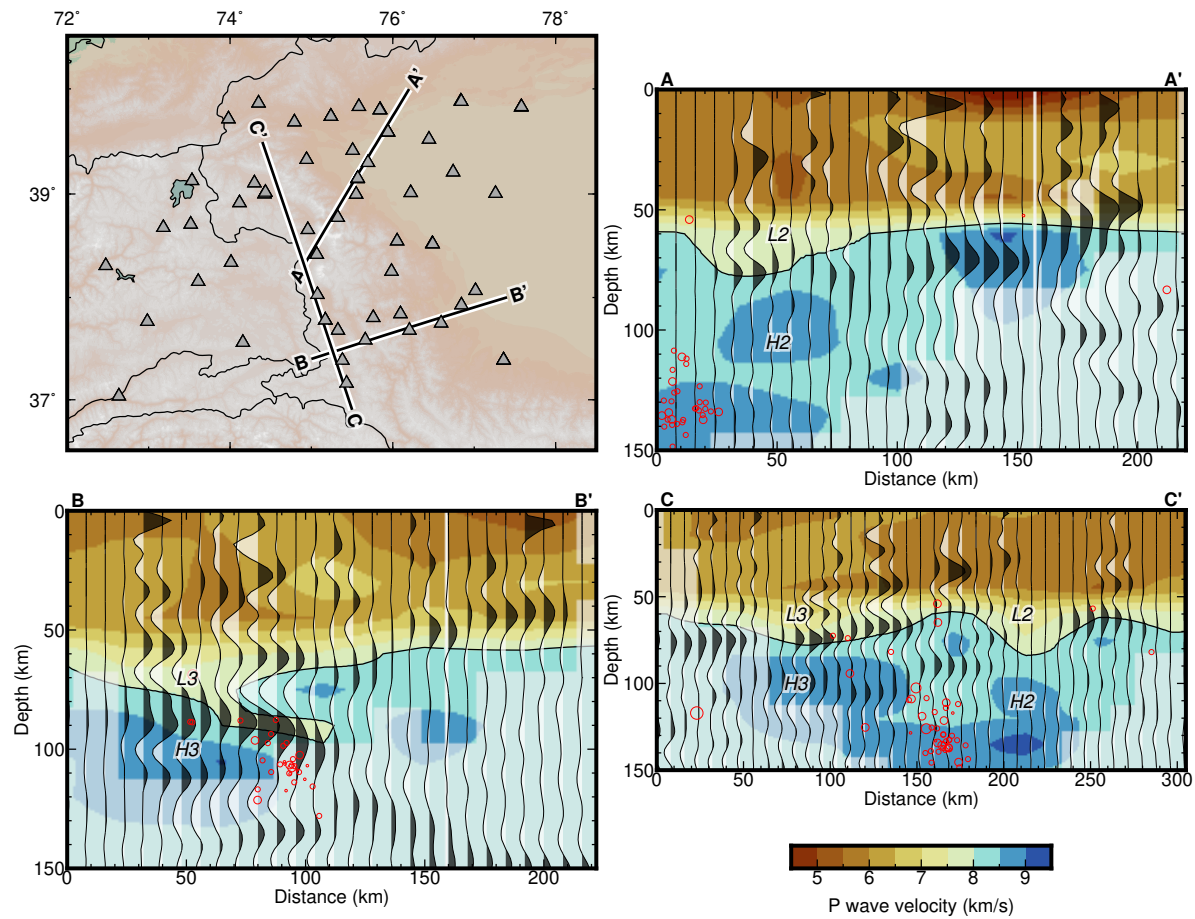


**Figure S16.** Profiles through the tomogram with common conversion point receiver function stacks along profiles of Xu et al. (2021) superimposed. Profile locations are guided by the station distribution and intersect the interpreted subsurface structures at oblique angles. The tomographic Moho (8 km/s contour) coincides in many places with the positive Moho conversion signal. The velocity contrasts  $L2/H2$  and  $L3/H3$  in the tomogram, that we interpret in the main article, show also a clear conversion signal.